Missouri University of Science and Technology
Scholars' Mine

Civil, Architectural and Environmental Engineering Faculty Research & Creative Works

Civil, Architectural and Environmental Engineering

01 Jan 2024

A Vehicle-bridge Interaction Model Considering Contact Patch Size And Vehicle Self-generated Excitation – A Theoretical Study

Zhenhua Shi

Yahya M. Mohammed

Nasim Uddin

Genda Chen
Missouri University of Science and Technology, gchen@mst.edu

Follow this and additional works at: https://scholarsmine.mst.edu/civarc_enveng_facwork

Part of the Structural Engineering Commons

Recommended Citation

Z. Shi et al., "A Vehicle-bridge Interaction Model Considering Contact Patch Size And Vehicle Self-generated Excitation – A Theoretical Study," *Engineering Structures*, vol. 298, article no. 117079, Elsevier, Jan 2024.
The definitive version is available at https://doi.org/10.1016/j.engstruct.2023.117079

This Article - Journal is brought to you for free and open access by Scholars' Mine. It has been accepted for inclusion in Civil, Architectural and Environmental Engineering Faculty Research & Creative Works by an authorized administrator of Scholars' Mine. This work is protected by U. S. Copyright Law. Unauthorized use including reproduction for redistribution requires the permission of the copyright holder. For more information, please contact scholarsmine@mst.edu.

Engineering Structures 298 (2024) 117079

Contents lists available at ScienceDirect

Engineering Structures

journal homepage: www.elsevier.com/locate/engstruct

A vehicle-bridge interaction model considering contact patch size and vehicle self-generated excitation – A theoretical study

Zhenhua Shi [a], Yahya M. Mohammed [b], Nasim Uddin [c], Genda Chen [a,*]

[a] Department of Civil, Architectural, and Environmental Engineering, Missouri University of Science and Technology, Rolla, MO 65409, USA
[b] Poepping, Stone, Bach, and Associates Inc., Quincy, IL 62305, USA
[c] Department of Civil, Construction and Environmental Engineering, The University of Alabama at Birmingham, Birmingham, AL 35294, USA

ARTICLE INFO

Keywords:
Contact patch
Vehicle bridge interaction
Natural frequency
Mode shape
Damping ratio
Vehicle excitation

ABSTRACT

This paper presents an improved theoretical damped single-axle vehicle-bridge dynamic interaction model to consider the effect of the contact patch size and motor-induced vehicle excitation. The contact patch issue is critical as it determines the minimum time step for simulation and maximum identifiable frequency, while the inclusion of the motor-induced vehicle excitation benefits the design of autonomous self-driven rather than towed vehicles. Estimations of the contact patch size for both the pneumatic tire and solid wheel scenarios are discussed. The contact patch responses, which degenerate into contact point responses when the contact patch size is assumed to be infinitely small, were derived for the first time both from the vehicle and bridge responses to confirm their equivalence. The minimum time step, which determines maximum identifiable frequency but is arbitrarily chosen in literature, is proposed to be determined by the vehicle speed and contact patch length. The procedures to extract multiple bridge triad information including natural frequencies, mode shapes, and damping ratios from the vehicle responses are also presented. Based on extensive parametric analyses, the sinusoidal vehicle excitation becomes more prominent as its amplitude and/or frequency increase and may overshadow the analysis of bridge frequencies of interest. The vehicle acceleration leads to a more accurate extraction of bridge mode shapes and damping ratios than the vehicle displacement since the displacement is dominated by the fundamental mode of bridge vibration. The damping ratio extraction shows an average error of 0.28% from the instantaneous amplitude of the vehicle acceleration signal.

1. Introduction

Vehicle-bridge interaction (VBI) has been widely studied in the past two decades. In 2004, Yang et al. [1] proposed a theoretical VBI model to extract the fundamental bridge frequency from the vibration response of a passing-by vehicle. Since then, both theoretical and experimental studies have been conducted to extract the natural frequencies [1-11], mode shapes [12-23], and damping properties [24-26] of the bridges from the vehicle responses. More recently, bridge dynamic characteristics have also been extracted from the vehicle-bridge contact point response [7-9,27,28]. Most of the research results have been summarized and reported in several review articles [20,29-34]. Despite extensive studies on the VBI topic, determining bridge modal properties from vehicle responses remains ineffective and unreliable, especially for the high-frequency vibration modes [20,29-33]. In the authors' opinion, the VBI mechanism is yet to be fully understood. In 2021, Shi and Uddin [35,36] showed that the low-frequency vehicle functioned like a filter to diminish the bridge responses associated with the bridge natural frequencies that are higher than the vehicle frequency. This theoretical observation was later experimentally confirmed by Yang et al. [9] in 2022 when they designed and compared a vehicle with polyurethane (PU) wheels and pneumatic rubber wheels. During their experiments, the vehicle with PU wheels showed no dominant frequencies up to 20 Hz, which was deemed to be a high-fidelity transmitter for the bridge modal attributes analysis.

The mode shapes of a bridge can also be extracted from vehicle responses as studied both theoretically and experimentally [12-23]. Yang et al. [12] extracted the mode shapes of a bridge from a passing-by vehicle when both the vehicle and bridge damping were neglected in their analytical model. Qi and Au [17] numerically reconstructed the mode shapes of girder bridges from the dynamic responses of a moving vehicle under impact excitations. The external impact excitation on the

* Corresponding author.
E-mail addresses: zhs@mst.edu (Z. Shi), yahyam@psba.com (Y.M. Mohammed), nuddin@uab.edu (N. Uddin), gchen@mst.edu (G. Chen).

https://doi.org/10.1016/j.engstruct.2023.117079
Received 22 June 2023; Received in revised form 11 October 2023; Accepted 19 October 2023
Available online 25 October 2023
0141-0296/© 2023 Elsevier Ltd. All rights reserved.

vehicle was necessary to ensure a significant robust interaction between the vehicle and the bridge. He et al. [18] extracted the fundamental, mass-normalized mode shape of an undamped bridge from experimental data. Based on Finite Element Model (FEM) and simulations, Nayek et al. [19] proposed a mode shape construction procedure using a single pair of moving actuator and sensor. Although experimentally extracting the eight mode shapes of a bridge with good accuracy, their approach used the data collected from the bridge, which lost the advantage of using vehicle data to extract bridge characteristics in a potentially more efficient way. The viewpoint that robust interaction between a vehicle and a bridge is beneficial to constructing the mode shapes of the bridge from the vehicle data was confirmed experimentally by Zhang et al. [20]. They installed bumps on an undamped beam structure and constructed the first two mode shapes of the structure from the dynamic response of a moving undamped mass. The bumps were believed to intensify a robust interaction between the moving mass and the beam. However, in field applications, the presence of bumps on a bridge will prevent a vehicle from running at high speed, besides, possible separation of the vehicle from the bridge due to the bumps may invalidate most, if not all, analytical models in the literature. Installing uniformly distributed bumps on a bridge is also costly and potentially affects the fatigue life of steel bridges. In another research, Zhang et al [21] constructed the first three mode shapes of a beam-like structure from the acceleration response of a moving lumped mass, which served as both an exciter and a moving sensor. The lumped mass directly rested on the structure without any spring and damping unit in between. Although quite different from a vehicle running across a highway bridge in practical applications, this experiment showed that the wheels play a critical role in transmitting the bridge dynamic information. He et, al. [22,23] recently used contact residual responses of multiple-connected vehicles to detect bridge modal parameters to reduce the effect of pavement irregularity. Compared to two-connected vehicle scenario with incomplete mode shape construction, the first three bridge modes could be constructed on a three-connected vehicle scenario. However, their models adopted contact point concept and did not consider the contact patch effect which affects the vehicle response due to pavement irregularity. The contact patch size determines the minimum time step and maximum identifiable frequencies of the VBI system and is believed to be playing a key role in the VBI mechanism.

The response of the contact point between a vehicle and a bridge was recently studied to extract the dynamic characteristics of the bridge with some advantages. In extraction of natural bridge frequencies, mode shapes, and damping ratios, Yang et al. [27] showed that the contact point response, due to its independence of the vehicle frequency, was advantageous over the undamped vehicle response. Xu et al. [7] considered the vehicle damping in their analytical model and identified the modal properties of an undamped bridge from the contact point response with experimental validations. Yang et al. [8] designed a single-axle vehicle with rocking motion to ensure that the contact point response was free of disturbance from natural frequencies of the vehicle. Yang et al. [28] further demonstrated that the contact point response of the rocking vehicle was not influenced by the road roughness. Xu et al. [37] recently proposed a closed-form solution for the contact point response of a single-axle two-spring-in-series vehicle and bridge interaction model to consider the effect of suspension. They also concluded that the contact point response outperformed the wheel response for the extraction of bridge dynamic characteristics. The contact point approach essentially preserves more bridge modal characteristics by averting the filtering effect of the vehicle's dynamic properties such as frequency and damping. This indicates that a sound interaction between the vehicle and bridge is necessary to transmit the bridge modal properties, especially high modes. However, the issue with contact point is that it leads to infinite interaction force and there will always be a contact patch instead in a physical world. The contact patch affects the vehicle response due to road irregularity as it could cancel out its effect if carefully designed, it also affects the minimum time step that is currently arbitrarily chosen in literature in numerical analysis. The contact patch plays a key role in transmitting the bridge modal properties to the vehicle response.

The above review indicates that the contact patch issue under vehicle weights hitherto has not been considered in previous VBI studies. In addition, the vehicle self-generated excitation due to engine vibration, driveshaft vibration, and high-speed vibration associated with unbalanced tire pressures and different tire wear-offs have not been considered in the formulation of theoretical analysis. These two factors are believed to play an important role in the understanding of the VBI mechanism. The length of a contact patch due to the deformation of the wheel may determine the maximum identifiable frequency of a bridge since the contact patch response represents an average of the responses of many contact points between the vehicle and the bridge. The response of a moving vehicle collected over a short time duration corresponding to the contact patch length may not be distinguishable as only overall response can be obtained. The vehicle self-generated excitation is notable. For instance, a 4-cylinder engine has two shakes (2 pistons on a power stroke) per revolution of a crankshaft, and a 6-cylinder (V-6) engine has three shakes per revolution of a crankshaft. They both would cause vibration on the vehicle. Understanding the effect of the external excitation is believed to be beneficial for designing autonomous self-driven vehicles compared to towed vehicles.

In this study, both the contact patch and the vehicle self-generated excitation are considered in a damped, single-axle vehicle bridge interaction model with multiple modal contributions. Two mathematical expressions for the contact point response are derived for the first time, both from the vehicle response and the bridge response, respectively, to demonstrate their equivalency. The insights on how to collect contact point responses are discussed. In parallel with this, the procedures to extract multiple bridge natural frequencies, mode shapes, and damping ratios from a vehicle response are presented. Note that due to the complexity of the mathematic expression, the heterogeneous irregularity on the bridge surface is not considered in this study, otherwise the closed-form solutions would not be obtained. The effect of road irregularity is usually tackled by FEM analysis but would not be verified by closed-form or explicit solutions, and thus is not the focus of this study. As pointed out earlier, the effect of road irregularity on the vehicle response will also be affected by the contact patch size. Section 2.3 discusses how to estimate contact patch length for different wheel materials and configurations. This paper is organized as follows. Section 2 presents the damped VBI model with closed-form solutions, equivalency of contact point responses from vehicle and bridge, discussion of contact patch length, and mode shape and damping ratio extraction. Section 3 compares the theoretical model with representative models in the literature and presents a series of parametric studies on the effect of excitation force and frequency, the attribute of contact point responses, and the extraction of mode shapes and damping ratios. Conclusions are drawn in Section 4.

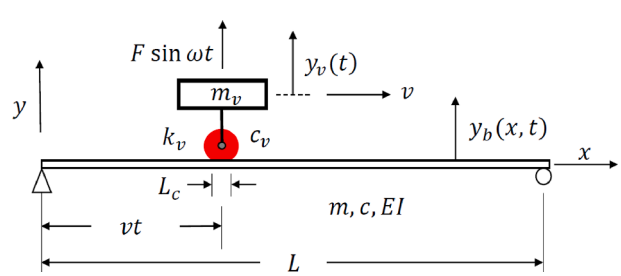

Fig. 1. An idealized vehicle-bridge interaction model.

2. Theoretical formulation

2.1. VBI model and analytical solution

Fig. 1 shows a schematic diagram of a damped, single-axle vehicle bridge interaction model with a contact patch at the vehicle-bridge interface under a vehicle self-generated excitation. The vehicle is represented by a spring-dashpot-mass oscillator with a mass of m_v, a damping constant of c_v, and a spring constant of k_v. The bridge is represented by a uniform Bernoulli-Euler beam with a constant mass per length of m, a constant damping coefficient per length of c, and a constant flexural stiffness of EI. The contact force on the vehicle-bridge interface is assumed to be uniformly distributed over a contact patch length of L_c due to the deformation of at the contact interface. The vehicle excitation over time t is represented by a sinusoidal force with an amplitude of F (peak force) and an excitation frequency of ω. Based on contact theory [38], the contact size depends on the moduli, Possion's ratios, radii, and the interaction force of the two interacting objects. Although the vehicle bridge interaction force consists of vehicle inertial force $m_v\ddot{y}_v$, external excitation force $Fsin\omega t$, and distributed vehicle weight $m_v g$, the contribution of the inertial force and external force is negligible which will be demonstrated in section 3.1. Thus, the contact length is assumed to be a constant, the estimation of which for both pneumatic and solid wheels will be discussed in section 2.3. The parameter L_c is critically important as it, together with a bridge length of L, determines the maximum sampling points along the bridge and thus the minimum time step given a vehicle speed of v, which is otherwise chosen arbitrarily in the literature.

Let the beam be defined along the x-axis of a x-y cartesian coordinate system. Consider statically equilibrium positions of both the vehicle and the bridge as the origins of their displacements, $y_v(t)$ and $y_b(x,t)$, respectively. Based on the D'Alembert's Principle [39], the coupled differential equations of motion for the VBI model can be expressed into

$$\begin{cases} m_v\ddot{y}_v + c_v\dot{y}_v + k_v y_v = k_v y_b|_{x=vt} + c_v\dfrac{\partial y_b}{\partial t}|_{x=vt} + Fsin\omega t \\ m\dfrac{\partial^2 y_b}{\partial t^2} + c\dfrac{\partial y_b}{\partial t} + EI\dfrac{\partial^4 y_b}{\partial x^4} = \begin{cases} \dfrac{-m_v\left(\ddot{y}_v + g\right) + Fsin\omega t}{L_c}, x = \left[vt - \dfrac{L_c}{2}, vt + \dfrac{L_c}{2}\right] \\ 0, x = \left[0, vt - \dfrac{L_c}{2}\right) \cup \left(vt + \dfrac{L_c}{2}, L\right] \end{cases} \end{cases} \tag{1}$$

in which $-m_v g$ is included in the bridge equation since $y_v(t)$ is originated from the statically equilibrium position of the vehicle and thus the bridge is subjected to a constant weight of the vehicle. Here, $\dot{y}_v$ and $\ddot{y}_v$ (first and second derivatives of the displacement) denote the velocity and acceleration of the vehicle, respectively. The mathematical operator $\partial y_b/\partial(.)$ represents partial derivative of the bridge displacement with respect to variable time t or space x. Let the bridge displacement $y_b(x,t)$ be expressed into a summation of an infinite number of the products of normal modes $\Phi_n(x)$ and modal coordinates $z_n(t)$ [39]. That is,

$$y_b(x,t) = \sum_n \Phi_n(x) z_n(t) \tag{2}$$

Substituting Eq. (2) into Eq. (1) and integrating the resulting equation over $x = [0, L]$ leads to

$$\begin{cases} \ddot{y}_v + 2\xi_v\omega_v\dot{y}_v + \omega_v^2 y_v = \dfrac{F}{m_v}sin\omega t + \sum_n\left[\omega_v^2 z_n(t) + 2\xi_v\omega_v\dot{z}_n(t)\right]\Phi_n(vt) \\ \ddot{z}_n(t) + 2\xi_n\omega_n\dot{z}_n(t) + \omega_n^2 z_n(t) = \dfrac{\int_{vt-L_c/2}^{vt+L_c/2}\Phi_n(x)\left[-m_v\left(\ddot{y}_v + g\right) + Fsin\omega t\right]dx}{mL_c\int_0^L \Phi_n^2(x)dx} \end{cases} \tag{3}$$

in which

$$2\xi_v\omega_v = \frac{c_v}{m_v}, 2\xi_n\omega_n = \frac{c}{m} \tag{4}$$

Note that the normal modes are for the bridge alone without presence of the vehicle and Eq. (2) is valid only when an infinite number of modes are included in theory. For a simply-supported bridge scenario, the nth normal mode can be expressed into

$$\Phi_n(x) = sin\frac{n\pi x}{L} \tag{5}$$

When $\ddot{y}_v \ll g$, the bridge equation can be uncoupled approximately. The second expression in Eq. (3) then becomes

$$\ddot{z}_n(t) + 2\xi_n\omega_n\dot{z}_n(t) + \omega_n^2 z_n(t) = p_n\left(-\frac{2m_v g}{mL}sin\frac{n\pi vt}{L} + \frac{F}{mL}cos\alpha_{n\omega}^{-}\frac{n\pi v}{L}t - \frac{F}{mL}cos\alpha_{n\omega}^{+}\frac{n\pi v}{L}t\right) \tag{6}$$

in which $\alpha_{n\omega}^{-} = 1 - \frac{\omega L}{n\pi v}$, $\alpha_{n\omega}^{+} = 1 + \frac{\omega L}{n\pi v}$, and the contact patch factor $p_n = [2L/(n\pi L_c)]sin[n\pi L_c/(2L)]$. As L_c/L approaches to zero, the contact patch factor approaches to 1. The solution to this second-order non-homogeneous differential equation (6) can be written as

$$\begin{aligned} z_n(t) = {} & e^{-\xi_n\omega_n t}(Q_n cos\omega_{nd}t + R_n sin\omega_{nd}t) + S_{n1}cos\frac{n\pi v}{L}t + T_{n1}sin\frac{n\pi v}{L}t \\ & + S_{n2}cos\alpha_{n\omega}^{-}\frac{n\pi v}{L}t - T_{n2}sin\alpha_{n\omega}^{-}\frac{n\pi v}{L}t + S_{n3}cos\alpha_{n\omega}^{+}\frac{n\pi v}{L}t + T_{n3}sin\alpha_{n\omega}^{+}\frac{n\pi v}{L}t \end{aligned} \tag{7}$$

in which $\omega_{nd} = \omega_n\sqrt{1-\xi_n^2}$ is the damped frequency of the bridge. Four pairs of coefficients (Q_n, R_n), (S_{n1}, T_{n1}), (S_{n2}, T_{n2}), and (S_{n3}, T_{n3}) are given in Appendix A. They define the transient response and three steady-state responses corresponding to the three terms on the right-hand side of Eq. (6). Once $z_n(t)$ is known, the bridge displacement and acceleration responses can be obtained from Eq. (2) as

$$y_b(x,t) = \sum_n \left\{ \begin{array}{l} e^{-\xi_n\omega_n t}[Q_n cos\omega_{nd}t + R_n sin\omega_{nd}t] \\ +S_{n1}cos\dfrac{n\pi v}{L}t + T_{n1}sin\dfrac{n\pi v}{L}t \\ +S_{n2}cos\alpha_{n\omega}^{-}\dfrac{n\pi v}{L}t - T_{n2}sin\alpha_{n\omega}^{-}\dfrac{n\pi v}{L}t \\ +S_{n3}cos\alpha_{n\omega}^{+}\dfrac{n\pi v}{L}t + T_{n3}sin\alpha_{n\omega}^{+}\dfrac{n\pi v}{L}t \end{array} \right\} sin\frac{n\pi x}{L} \tag{8}$$

$$\frac{\partial^2 y_b(x,t)}{\partial t^2}=\sum_n\left\{\begin{array}{c} e^{-\xi_n\omega_n t}\left[\begin{array}{c}\left[(\xi_n\omega_n)^2Q_n-2\xi_n\omega_nR_n\omega_{nd}-Q_n\omega_{nd}^2\right]cos\omega_{nd}t\\ +\left[(\xi_n\omega_n)^2R_n+2\xi_n\omega_nQ_n\omega_{nd}-R_n\omega_{nd}^2\right]sin\omega_{nd}t\end{array}\right]\\ -S_{n1}\left(\frac{n\pi v}{L}\right)^2cos\frac{n\pi v}{L}t-T_{n1}\left(\frac{n\pi v}{L}\right)^2sin\frac{n\pi v}{L}t\\ -S_{n2}\left(\alpha_{n\omega}^-\frac{n\pi v}{L}\right)^2cos\alpha_{n\omega}^-\frac{n\pi v}{L}t+T_{n2}\left(\alpha_{n\omega}^-\frac{n\pi v}{L}\right)^2sin\alpha_{n\omega}^-\frac{n\pi v}{L}t\\ -S_{n3}\left(\alpha_{n\omega}^+\frac{n\pi v}{L}\right)^2cos\alpha_{n\omega}^+\frac{n\pi v}{L}t-T_{n3}\left(\alpha_{n\omega}^+\frac{n\pi v}{L}\right)^2sin\alpha_{n\omega}^+\frac{n\pi v}{L}t\end{array}\right\}sin\frac{n\pi x}{L} \tag{9}$$

Eqs. (8) and (9) show several frequency components included in the bridge responses. They are the damped bridge frequency ω_{nd}, vehicle driving frequency $n\pi v/L$, and two excitation-affected vehicle driving frequencies $\alpha_{n\omega}^-n\pi v/L$ and $\alpha_{n\omega}^+n\pi v/L$. Substituting the expressions of $z_n(t)$ and $\Phi_n(x)$ into the equation for the vehicle in Eq. (3) yields

$$\ddot{y}_v+2\xi_v\omega_v\dot{y}_v+\omega_v^2y_v=\frac{F}{m_v}sin\omega t+\frac{1}{2}\sum_n\left\{\begin{array}{c} b_n^*e^{-\xi_n\omega_n t}cos\beta_{n\omega_{nd}}^-\frac{n\pi v}{L}t\\ -b_n^*e^{-\xi_n\omega_n t}cos\beta_{n\omega_{nd}}^+\frac{n\pi v}{L}t\\ +a_n^*e^{-\xi_n\omega_n t}sin\beta_{n\omega_{nd}}^+\frac{n\pi v}{L}t\\ +a_n^*e^{-\xi_n\omega_n t}sin\beta_{n\omega_{nd}}^-\frac{n\pi v}{L}t\\ -d_n^*cos\frac{2n\pi v}{L}t+c_n^*sin\frac{2n\pi v}{L}t\\ +\left(h_n^*-f_n^*\right)cos\omega t+\left(e_n^*-g_n^*\right)sin\omega t\\ +f_n^*cos\alpha_{2n\omega}^-\frac{2n\pi v}{L}t+e_n^*sin\alpha_{2n\omega}^-\frac{2n\pi v}{L}t\\ -h_n^*cos\alpha_{2n\omega}^+\frac{2n\pi v}{L}t+g_n^*sin\alpha_{2n\omega}^+\frac{2n\pi v}{L}t\\ +d_n^*\end{array}\right\} \tag{10}$$

in which $\alpha_{2n\omega}^-=1-\omega L/2n\pi v$, $\alpha_{2n\omega}^+=1+\omega L/2n\pi v$, $\beta_{n\omega_{nd}}^-=1-\omega_{nd}L/n\pi v$, $\beta_{n\omega_{nd}}^+=1+\omega_{nd}L/n\pi v$, and

$$\left\{\begin{array}{l} a_n^*=\omega_v^2Q_n-2\xi_v\omega_v\xi_n\omega_nQ_n+2\xi_v\omega_vR_n\omega_{nd}\\ b_n^*=\omega_v^2R_n-2\xi_v\omega_v\xi_n\omega_nR_n-2\xi_v\omega_vQ_n\omega_{nd}\\ c_n^*=\omega_v^2S_{n1}+2\xi_v\omega_vT_{n1}\frac{n\pi v}{L}\\ d_n^*=\omega_v^2T_{n1}-2\xi_v\omega_vS_{n1}\frac{n\pi v}{L}\\ e_n^*=\omega_v^2S_{n2}-2\xi_v\omega_vT_{n2}\alpha_{n\omega}^-\frac{n\pi v}{L}\\ f_n^*=\omega_v^2T_{n2}+2\xi_v\omega_vS_{n2}\alpha_{n\omega}^-\frac{n\pi v}{L}\\ g_n^*=\omega_v^2S_{n3}+2\xi_v\omega_vT_{n3}\alpha_{n\omega}^+\frac{n\pi v}{L}\\ h_n^*=\omega_v^2T_{n3}-2\xi_v\omega_vS_{n3}\alpha_{n\omega}^+\frac{n\pi v}{L}\end{array}\right. \tag{11}$$

The vehicle displacement and acceleration responses can then be determined as

$$y_v=e^{-\xi_v\omega_v t}\left(\begin{array}{c}U_1\cos\omega_{vd}t\\ +V_1\sin\omega_{vd}t\end{array}\right)+\left(\begin{array}{c}U_2\cos\omega t\\ +V_2\sin\omega t\end{array}\right)$$
$$+\frac{1}{2}\sum_n\left\{\begin{array}{c} +e^{-\xi_n\omega_n t}\left(\begin{array}{c}M_{n3}\cos\beta_{n\omega_{nd}}^-\frac{n\pi v}{L}t-N_{n3}\sin\beta_{n\omega_{nd}}^-\frac{n\pi v}{L}t\\ +M_{n4}\cos\beta_{n\omega_{nd}}^+\frac{n\pi v}{L}t+N_{n4}\sin\beta_{n\omega_{nd}}^+\frac{n\pi v}{L}t\end{array}\right)\\ +M_{n5}\cos\frac{2n\pi v}{L}t+N_{n5}\sin\frac{2n\pi v}{L}t\\ +M_{n7}\cos\alpha_{2n\omega}^-\frac{2n\pi v}{L}t-N_{n7}\sin\alpha_{2n\omega}^-\frac{2n\pi v}{L}t\\ +M_{n8}\cos\alpha_{2n\omega}^+\frac{2n\pi v}{L}t+N_{n8}\sin\alpha_{2n\omega}^+\frac{2n\pi v}{L}t\\ +\frac{d_n^*}{\omega_v^2}\end{array}\right\} \tag{12}$$

$$\ddot{y}_v(t) = e^{-\xi_v\omega_v t}\begin{Bmatrix} \left[(\xi_v\omega_v)^2 U_1 - 2\xi_v\omega_v\omega_{vd}V_1 - U_1\omega_{vd}^2\right]cos\omega_{vd}t \\ \left[(\xi_v\omega_v)^2 V_1 + 2\xi_v\omega_v\omega_{vd}U_1 - V_1\omega_{vd}^2\right]sin\omega_{vd}t \end{Bmatrix} - \begin{pmatrix} U_2\omega^2 cos\omega t \\ +V_2\omega^2 sin\omega t \end{pmatrix}$$

$$+\frac{1}{2}\sum_n \left\{ \begin{array}{c} +e^{-\xi_n\omega_n t}\left\{ \begin{array}{c} \left[(\xi_n\omega_n)^2 M_{n3} + 2\xi_n\omega_n N_{n3}\beta^-_{n\omega_{nd}}\frac{n\pi v}{L} - M_{n3}\left(\beta^-_{n\omega_{nd}}\frac{n\pi v}{L}\right)^2\right]cos\beta^-_{n\omega_{nd}}\frac{n\pi v}{L}t \\ -\left[(\xi_n\omega_n)^2 N_{n3} - 2\xi_n\omega_n M_{n3}\beta^-_{n\omega_{nd}}\frac{n\pi v}{L} - N_{n3}\left(\beta^-_{n\omega_{nd}}\frac{n\pi v}{L}\right)^2\right]sin\beta^-_{n\omega_{nd}}\frac{n\pi v}{L}t \\ +\left[(\xi_n\omega_n)^2 M_{n4} - 2\xi_n\omega_n N_{n4}\beta^+_{n\omega_{nd}}\frac{n\pi v}{L} - M_{n4}\left(\beta^+_{n\omega_{nd}}\frac{n\pi v}{L}\right)^2\right]cos\beta^+_{n\omega_{nd}}\frac{n\pi v}{L}t \\ +\left[(\xi_n\omega_n)^2 N_{n4} + 2\xi_n\omega_n M_{n4}\beta^+_{n\omega_{nd}}\frac{n\pi v}{L} - N_{n4}\left(\beta^+_{n\omega_{nd}}\frac{n\pi v}{L}\right)^2\right]sin\beta^+_{n\omega_{nd}}\frac{n\pi v}{L}t \end{array} \right\} \\ -M_{n5}\left(\frac{2n\pi v}{L}\right)^2 cos\frac{2n\pi v}{L}t - N_{n5}\left(\frac{2n\pi v}{L}\right)^2 sin\frac{2n\pi v}{L}t \\ -M_{n7}\left(\alpha^-_{2n\omega}\frac{2n\pi v}{L}\right)^2 cos\alpha^-_{2n\omega}\frac{2n\pi v}{L}t + N_{n7}\left(\alpha^-_{2n\omega}\frac{2n\pi v}{L}\right)^2 sin\alpha^-_{2n\omega}\frac{2n\pi v}{L}t \\ -M_{n8}\left(\alpha^+_{2n\omega}\frac{2n\pi v}{L}\right)^2 cos\alpha^+_{2n\omega}\frac{2n\pi v}{L}t - N_{n8}\left(\alpha^+_{2n\omega}\frac{2n\pi v}{L}\right)^2 sin\alpha^+_{2n\omega}\frac{2n\pi v}{L}t \end{array} \right\} \tag{13}$$

in which $\omega_{vd} = \omega_v\sqrt{1-\xi_v^2}$ is the damped vehicle frequency. Nine pairs of coefficients (U_1, V_1), (U_2, V_2), (M_{n2}, N_{n2}), (M_{n3}, N_{n3}), (M_{n4}, N_{n4}), (M_{n5}, N_{n5}), (M_{n6}, N_{n6}), (M_{n7}, N_{n7}), and (M_{n8}, N_{n8}) are summarized in Appendix B. Note that in Eq. (13) for conciseness, (M_{n2}, N_{n2}) and (M_{n6}, N_{n6}) are incorporated in (U_1, V_1) and (U_2, V_2), respectively. The frequency components that affect the vehicle response include the vehicle self-generated excitation frequency ω, damped vehicle frequency ω_{vd}, driving frequency affected damped bridge frequencies $\omega_{nd} \pm n\pi v/L$, doubled driving frequency $2n\pi v/L$, and excitation-affected doubled driving frequencies $\alpha^-_{2n\omega}2n\pi v/L$ and $\alpha^+_{2n\omega}2n\pi v/L$. All these frequency components ought to be carefully related to their sources during frequency analysis. The camel hump phenomenon related to the vehicle self-generated excitation frequency is expected from both the vehicle responses ($\alpha^\pm_{2n\omega}\frac{2n\pi v}{L}$) and the bridge responses ($\alpha^\pm_{n\omega}\frac{n\pi v}{L}$), while that related to the bridge frequencies will only be expected from vehicle responses ($\beta^\pm_{n\omega_{nd}}\frac{n\pi v}{L}$).

2.2. Contact point response

The contact point concept was originally proposed by Yang [27] in 2018 to exclude the effect of vehicle frequency during the extraction of the bridge modal characteristics, but the derivations from both the vehicle and bridge response have not yet been confirmed equivalent. The contact point response is essentially the bridge response at the location of the vehicle as it passes on the bridge, which can be derived either by letting $x = vt$ in the bridge response in Eq. (8) or by letting $k_v \to \infty$, $c_v \to 0$ and $m_v \neq 0$ in the vehicle response in Eq. (12). These two approaches have been proven equivalent, leading to the same contact point displacement response as shown in Eq. (14). The double derivative of the displacement response gives the contact point acceleration response as presented in Eq. (15).

$$y_c(t) = \frac{1}{2}\sum_n \left\{ \begin{array}{c} e^{-\xi_n\omega_n t}\begin{bmatrix} R_n cos\beta^-_{n\omega_{nd}}\frac{n\pi v}{L}t + Q_n sin\beta^-_{n\omega_{nd}}\frac{n\pi v}{L}t \\ -R_n cos\beta^+_{n\omega_{nd}}\frac{n\pi v}{L}t + Q_n sin\beta^+_{n\omega_{nd}}\frac{n\pi v}{L}t \end{bmatrix} \\ -T_{n1}cos\frac{2n\pi vt}{L} + S_{n1}sin\frac{2n\pi vt}{L} \\ +(T_{n3} - T_{n2})cos\omega t + (S_{n2} - S_{n3})sin\omega t \\ +T_{n2}cos\alpha^-_{2n\omega}\frac{2n\pi v}{L}t + S_{n2}sin\alpha^-_{2n\omega}\frac{2n\pi v}{L}t \\ -T_{n3}cos\alpha^+_{2n\omega}\frac{2n\pi v}{L}t + S_{n3}sin\alpha^+_{2n\omega}\frac{2n\pi v}{L}t \\ +T_{n1} \end{array} \right\} \tag{14}$$

$$\ddot{y}_c(t) = \frac{1}{2}\sum_n \left\{ \begin{array}{c} e^{-\xi_n\omega_n t}\left\{ \begin{array}{c} \left[(\xi_n\omega_n)^2 R_n - 2\xi_n\omega_n Q_n \beta^-_{n\omega_{nd}}\frac{n\pi v}{L} - R_n\left(\beta^-_{n\omega_{nd}}\frac{n\pi v}{L}\right)^2\right] cos\beta^-_{n\omega_{nd}}\frac{n\pi v}{L}t \\ +\left[(\xi_n\omega_n)^2 Q_n + 2\xi_n\omega_n R_n \beta^-_{n\omega_{nd}}\frac{n\pi v}{L} - Q_n\left(\beta^-_{n\omega_{nd}}\frac{n\pi v}{L}\right)^2\right] sin\beta^-_{n\omega_{nd}}\frac{n\pi v}{L}t \\ -\left[(\xi_n\omega_n)^2 R_n + 2\xi_n\omega_n Q_n \beta^+_{n\omega_{nd}}\frac{n\pi v}{L} - R_n\left(\beta^+_{n\omega_{nd}}\frac{n\pi v}{L}\right)^2\right] cos\beta^+_{n\omega_{nd}}\frac{n\pi v}{L}t \\ +\left[(\xi_n\omega_n)^2 Q_n - 2\xi_n\omega_n R_n \beta^+_{n\omega_{nd}}\frac{n\pi v}{L} - Q_n\left(\beta^+_{n\omega_{nd}}\frac{n\pi v}{L}\right)^2\right] sin\beta^+_{n\omega_{nd}}\frac{n\pi v}{L}t \end{array} \right\} \\ +T_{n1}\left(\frac{2n\pi v}{L}\right)^2 cos\frac{2n\pi v}{L}t - S_{n1}\left(\frac{2n\pi v}{L}\right)^2 sin\frac{2n\pi v}{L}t \\ -(T_{n3}-T_{n2})\omega^2 cos\omega t - (S_{n2}-S_{n3})\omega^2 sin\omega t \\ -T_{n2}\left(\alpha^-_{2n\omega}\frac{2n\pi v}{L}\right)^2 cos\alpha^-_{2n\omega}\frac{2n\pi v}{L}t - S_{n2}\left(\alpha^-_{2n\omega}\frac{2n\pi v}{L}\right)^2 sin\alpha^-_{2n\omega}\frac{2n\pi v}{L}t \\ +T_{n3}\left(\alpha^+_{2n\omega}\frac{2n\pi v}{L}\right)^2 cos\alpha^+_{2n\omega}\frac{2n\pi v}{L}t - S_{n3}\left(\alpha^+_{2n\omega}\frac{2n\pi v}{L}\right)^2 sin\alpha^+_{2n\omega}\frac{2n\pi v}{L}t \end{array} \right\} \tag{15}$$

2.3. Contact patch length

In a physical VBI system, the contact point turns into a contact patch issue due to the deformation at the contact interface between the wheel and the bridge surface, otherwise, the interaction force would be infinite. This subsection briefly discusses how to estimate the contact length for different types of wheels. For pneumatic tire, the contact patch size mainly depends on the distributed weight and the pressure difference. If designate d_v as the tire section width along the wheel axle direction (perpendicular to travel direction), p and p_0 respectively as the inflated tire pressure and atmospheric pressure (101 kPa), and $m_v g$ as the weight that distributed on the tire. The contact patch length can be estimated as

$$L_c = \frac{m_v g}{d_v(p - p_0)} \tag{16}$$

For instance, if using parameters from studies by Behroozinia et al. [40], for a pneumatic tire with a section width of 0.265 m, inflated pressure of 206 kPa, and a distributed vehicle weight of 4000 N, the contact patch length can be calculated as 0.144 m, which is only 0.69% of difference compared to their FEM result of 0.143 m, and 4.17% of difference compared to their estimated length of 0.138 m obtained from circumferential acceleration peaks from experiment. However, for a solid wheel scenario, the contact length could be roughly approximated based on Hertzian contact theory as [38]

$$L_c = 4\sqrt{\frac{m_v g R}{\pi d_v E^*}} \tag{17}$$

in which R is the radius of the wheel, equivalent E^* is calculated as

$$\frac{1}{E^*} = \frac{1-\nu_1^2}{E_1} + \frac{1-\nu_2^2}{E_2} \tag{18}$$

in which E_1,ν_1 and E_2,ν_2 are the elastic modulus and Possion's ratio of the wheel and the flat surface, respectively.

Eq. (17) shows that wheel size affects contact patch length. Yang and Cao [10], and Yang and Feng [11] proposed multiple-mass VBI models to consider the size of the wheel, but their studies still adopted contact point concept and did not relate the wheel size to the contact patch size that determines the minimum time step (0.001s is commonly used in numerical and FEM case studies) which eventually determines the maximum identifiable frequencies from the VBI system. Understanding of this issue helps design effective VBI system, especially for detecting high modal bridge parameters from the vehicle response.

Since the collected signal from the vehicle represents the average effect of many contact points over the contact patch, the minimum time step Δt over which the bridge information can be reliably discerned depends upon the vehicle speed v and the contact patch length L_c. This relationship and its corresponding maximum identifiable frequency f_{max} are presented in Eq. (19). To increase the maximum identifiable frequency, one may need to design a special wheel so that the contact patch length is reduced as much as possible. In theory, one could also increase the vehicle speed. However, a high-speed vehicle introduces significant camel hump phenomenon, shortens signal length, and increases the signal magnitude that may nullify the assumption $\ddot{y}_v \ll g$. Table 1 compares different contact patch lengths and maximum identifiable

Table 1
Contact patch lengths and maximum identifiable frequencies for different wheel materials.

Material	E_1(N·m^{-2})	Poisson's ratio ν_1	L_c(m)	f_{max}(Hz)
Steel	2.1×10^{11}	0.28	8.51×10^{-4}	5250
Aluminum	6.9×10^{10}	0.33	9.60×10^{-4}	4657
PU	5.0×10^{9}	0.4	2.12×10^{-3}	2108
Rubber	1.0×10^{7}	0.5	4.16×10^{-2}	107
Pneumatic	N/A	N/A	0.144	31

Note: Contact patch length for pneumatic scenario is calculated based on Eq. (16).

frequencies for common wheel materials using parameters of $m_v g = 4000N$, $R = 0.3m$, $d_v = 0.265$ m, $E_2 = 3.549 \times 10^{10}$ N·m^{-2}, $\nu_2 = 0.2$, and vehicle speed of $v = 8.941$ m·s^{-1}. Compared to solid wheel scenarios, pneumatic tire induces larger contact patch length and significant lower maximum identifiable frequency. To collect the contact point signal with maximum identifiable frequency in physical application, one idealized approach is to install sensors on the solid wheel of a specially-designed undamped vehicle such that $k_v \to \infty$ and $c_v \to 0$.

$$\begin{cases} f_{max} = \dfrac{1}{2\Delta t} \\ \Delta t = \dfrac{L_c}{v} \end{cases} \tag{19}$$

2.4. Mode shape and damping ratio

A three-step procedure is developed to extract the mode shapes and damping ratios of the bridge. In the first step, the vehicle response (either displacement or acceleration) or the contact point signal is decomposed so that only one mode of the bridge vibration with one natural frequency is included. Take the vehicle acceleration response in Eq. (13) as an example. The nth decomposed acceleration response of the vehicle is (this would also be the case if derived from the contact point response)

$$\ddot{y}_v(t)|_{bn} = e^{-\xi_n \omega_n t} \left\{ \begin{array}{l} \left[(\xi_n\omega_n)^2 M_{n3} + 2\xi_n\omega_n N_{n3}\beta^-_{n\omega_{nd}}\dfrac{n\pi v}{L} - M_{n3}\left(\beta^-_{n\omega_{nd}}\dfrac{n\pi v}{L}\right)^2 \right] cos\beta^-_{n\omega_{nd}}\dfrac{n\pi v}{L}t \\ -\left[(\xi_n\omega_n)^2 N_{n3} - 2\xi_n\omega_n M_{n3}\beta^-_{n\omega_{nd}}\dfrac{n\pi v}{L} - N_{n3}\left(\beta^-_{n\omega_{nd}}\dfrac{n\pi v}{L}\right)^2 \right] sin\beta^-_{n\omega_{nd}}\dfrac{n\pi v}{L}t \\ +\left[(\xi_n\omega_n)^2 M_{n4} - 2\xi_n\omega_n N_{n4}\beta^+_{n\omega_{nd}}\dfrac{n\pi v}{L} - M_{n4}\left(\beta^+_{n\omega_{nd}}\dfrac{n\pi v}{L}\right)^2 \right] cos\beta^+_{n\omega_{nd}}\dfrac{n\pi v}{L}t \\ +\left[(\xi_n\omega_n)^2 N_{n4} + 2\xi_n\omega_n M_{n4}\beta^+_{n\omega_{nd}}\dfrac{n\pi v}{L} - N_{n4}\left(\beta^+_{n\omega_{nd}}\dfrac{n\pi v}{L}\right)^2 \right] sin\beta^+_{n\omega_{nd}}\dfrac{n\pi v}{L}t \end{array} \right\} \tag{20}$$

Within the speed limit on highways, the vehicle driving frequency is typically less than 5% of the fundamental bridge frequency and significantly lesser for higher bridge modes. When $n\pi v/L \ll \omega_{nd}$, $M_{n3} = -M_{n4}$ and $N_{n3} = -N_{n4}$ as can be seen from Appendix B. The above expression becomes

$$\ddot{y}_v(t)|_{bn} = e^{-\xi_n \omega_n t} \begin{pmatrix} k_n cos\beta^-_{n\omega_{nd}}\dfrac{n\pi v}{L}t + l_n sin\beta^-_{n\omega_{nd}}\dfrac{n\pi v}{L}t \\ -k_n cos\beta^+_{n\omega_{nd}}\dfrac{n\pi v}{L}t + l_n sin\beta^+_{n\omega_{nd}}\dfrac{n\pi v}{L}t \end{pmatrix} \tag{21}$$

in which

$$\begin{cases} k_n = \left[2N_{n4}\xi_n\sqrt{1-\xi_n^2} - (2\xi_n^2 - 1)M_{n4} \right]\omega_n^2 \\ l_n = \left[2M_{n4}\xi_n\sqrt{1-\xi_n^2} + (2\xi_n^2 - 1)N_{n4} \right]\omega_n^2 \end{cases} \tag{22}$$

In the second step, Hilbert Transform is introduced to form an analytic function of the acceleration response and its instantaneous amplitude and phase, which is advantageous in averting aliasing effects in band-pass signal processing. Hilbert Transform can transform a time sequence $x(t)$ into its orthogonal counterpart with a 90° phase shift as designated as $\hat{x}(t) = H[x(t)]$. An analytic function $\psi(t)$ in a complex plane [41] can then be expressed into

$$\psi(t) = x(t) + i\hat{x}(t) = A(t)e^{-i\varphi(t)} \tag{23}$$

in which the instantaneous amplitude $A(t)$ and phase $\varphi(t)$ are respectively defined as

$$A(t) = \sqrt{x^2(t) + \hat{x}^2(t)}, \varphi(t) = arctan\frac{\hat{x}(t)}{x(t)} \tag{24}$$

After $H(sin\omega t) = -cos\omega t$ and $H(cos\omega t) = sin\omega t$ are introduced, the Hilbert Transform of the decomposed vehicle acceleration response in Eq. (21) becomes

$$\ddot{y}_v(t)|_{\hat{b}n} = e^{-\xi_n \omega_n t} \begin{pmatrix} -k_n sin\beta^-_{n\omega_{nd}}\dfrac{n\pi v}{L}t + l_n cos\beta^-_{n\omega_{nd}}\dfrac{n\pi v}{L}t \\ -k_n sin\beta^+_{n\omega_{nd}}\dfrac{n\pi v}{L}t - l_n cos\beta^+_{n\omega_{nd}}\dfrac{n\pi v}{L}t \end{pmatrix} \tag{25}$$

The instantaneous amplitude of the vehicle acceleration response can then be constructed as

$$A_{\ddot{y}_v}(t) = \sqrt{\left[\ddot{y}_v(t)|_{bn}\right]^2 + \left[\ddot{y}_v(t)|_{\hat{b}n}\right]^2} = 2\sqrt{k_n^2 + l_n^2}e^{-\xi_n\omega_n t}\left|sin\frac{n\pi v t}{L}\right| \tag{26}$$

Similarly, the instantaneous amplitude of the vehicle displacement response can be expressed into

$$A_{y_v}(t) = \sqrt{\left[y_v(t)|_{bn}\right]^2 + \left[y_v(t)|_{\hat{b}n}\right]^2} = 2\sqrt{M_{n4}^2 + N_{n4}^2}\, e^{-\xi_n\omega_n t}\left|sin\frac{n\pi v t}{L}\right| \tag{27}$$

In the third step, the instantaneous amplitude is used to determine the mode shape and damping ratio of the bridge. Notably from Eq. (26) or (27), the instantaneous amplitude contains the magnitude of the mode shape $|sin(n\pi vt/L)|$ and damping ratio ξ_n of the bridge. By examining the relative phases among various locations of the bridge, the mode shape of the bridge corresponding to each natural frequency can be constructed [42]. To extract the damping ratio, the logarithmic decrement method [39] can be applied to two peaks of the instantaneous amplitude. The two consecutive peaks A_1 and A_2 on the instantaneous amplitude are

Table 2
Vehicle and bridge parameters used in benchmark study.

Vehicle Property		Bridge Property	
k_v(N·m^{-1})	8.058×10^{10}	EI(N·m^2)	5.070×10^{10}
m_v(kg)	2.268×10^4	m(kg·m^{-1})	1.878×10^3
ξ_v	0.2	ξ_b	0.02
v(m·s^{-1})	8.941	L(m)	30.48
f_v(Hz)	300	f_b(1st- 5th) (Hz)	8.785, 35.14, 79.06, 140.56, 219.6

separated for a period of $\Delta t = L/(nv)$, the damping ratio can be calculated from the following expression:

$$\xi_n = \frac{1}{\omega_n \Delta t} ln \frac{A_1}{A_2} \tag{28}$$

Even though the first mode does not have two consecutive peaks, the damping ratio can still be calculated using the instantaneous amplitude at the quarter time point $t_{1/4}$ and third-quarter time point $t_{3/4}$ of the collected signal:

$$\xi_1 = \frac{1}{\omega_1 \left(t_{3/4} - t_{1/4}\right)} ln \frac{A_{1/4}}{A_{3/4}} \tag{29}$$

in which $A_{1/4}$ and $A_{3/4}$ are the instantaneous amplitudes at the quarter time point $t_{1/4}$ and third-quarter time point $t_{3/4}$, respectively. In theory, $t_{1/4} = L/(4v)$ and $t_{3/4} = 3L/(4v)$.

3. Parametric studies

3.1. Benchmark model parameters

The vehicle and bridge parameters as summarized in Table 2 are mainly adapted from studies by Shi and Uddin [35,36] in which they adopted AASHTO HL-93 design tandem load (50 kips in total) as an equivalent single axle vehicle example, and a prestressed girder bridge as an equivalent simply support bridge example [43]. They studied the effect of bridge damping, vehicle damping, frequency, speed, and mass for various bridge boundary conditions. One of their major findings is that the vehicle frequency should be higher than the bridge frequencies of interest to minimize any 'filtering' effect on vehicle responses. Vehicle with such a frequency design is referred to as frequency-free vehicle by Yang et al. [9]. Specifically, they used solid PU tires on a special vehicle for bridge modal retrieval. Note that the mathematical model and its solutions presented in this paper are not limited to any specific example so long as $\ddot{y}_v \ll g$. For example, special cases with zero excitation force and frequency as well as zero vehicle and bridge damping agree well with the results reported in the literature using their parameters [3,27] or equivalent parameters [37].

Table 3
Frequency analysis of single-axle vehicles without and with self-generated excitations.

Theoretical frequency (Hz)	Vehicle without self-excitation		Vehicle with self-excitation	
	Frequency (Hz)	Error (%)	Frequency (Hz)	Error (%)
8.785	8.798	0.15%	8.798	0.15%
35.14	35.19	0.15%	35.19	0.15%
50 (excitation)	N/A	N/A	49.86	0.28%
79.06	79.18	0.15%	79.18	0.15%
140.6	140.5	0.06%	140.5	0.06%
219.6	219.7	0.02%	219.7	0.02%

Note: Bridge frequencies are identified at the trough due to camel hump phenomenon.

In addition, the peak force is assumed as 1% of the total weight of a typical engine of 500 lbs (226.8 kg), namely $F = 22.24$ N, and the excitation frequency is based on $\omega = 50$ Hz to account for a 3000 Revolutions-Per-Minute (RPM) of rotation. Notably here, the interaction force between the vehicle and the bridge due to inertial force ($\ddot{y}_v \ll g$) and external excitation (22.24 N) is negligible compared to the vehicle weight (2.224×10^5 N), thus the assumption of constant contact patch length is reasonable. The contact patch length, which could be adjusted by changing wheel materials and configurations, is initially chosen as L_c = ¼ in (6.35×10^{-3} m) so that the minimum time step Δt can be set to 7.1×10^{-4} s, resulting in a maximum frequency identification of 704 Hz. The maximum number of points along the bridge is determined by L/L_c. The derived formulas are programmed and implemented on MATLAB platform [44].

3.2. Effects of peak force and excitation frequency

The peak force and excitation frequency play a certain role in the bridge frequency extraction from the vehicle acceleration signal. The vehicle excitation frequency may shed light on why it is difficult to identify bridge frequencies from the vehicle acceleration signal. As an extreme example, Fig. 2 compares the acceleration signal and corresponding frequency analyses of the vehicle without self-excitation and those with self-excitation (ω = 50 Hz, F = 2,224 N, 100% of engine weight). The acceleration signal strength with excitation (0.2586 m·s^{-2}) is approximately 2 times as much as that without excitation (0.1295 m·s^{-2}). Although multiple bridge frequencies could be identified in both scenarios as summarized in Table 3, the vehicle excitation frequency overshadows the presence of other frequency components. The

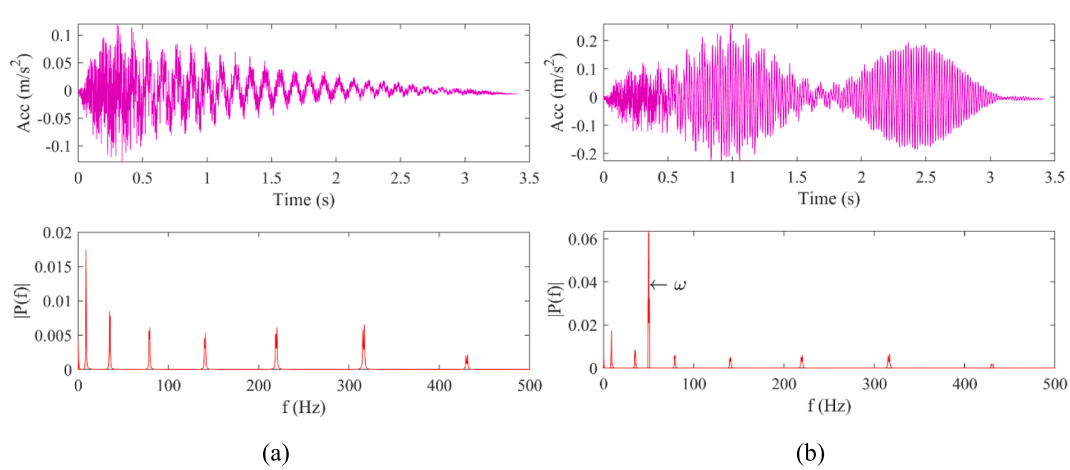

Fig. 2. Acceleration response and Fourier spectrum of a vehicle: (a) Without self-generated excitation and (b) With self-generated excitation ω.

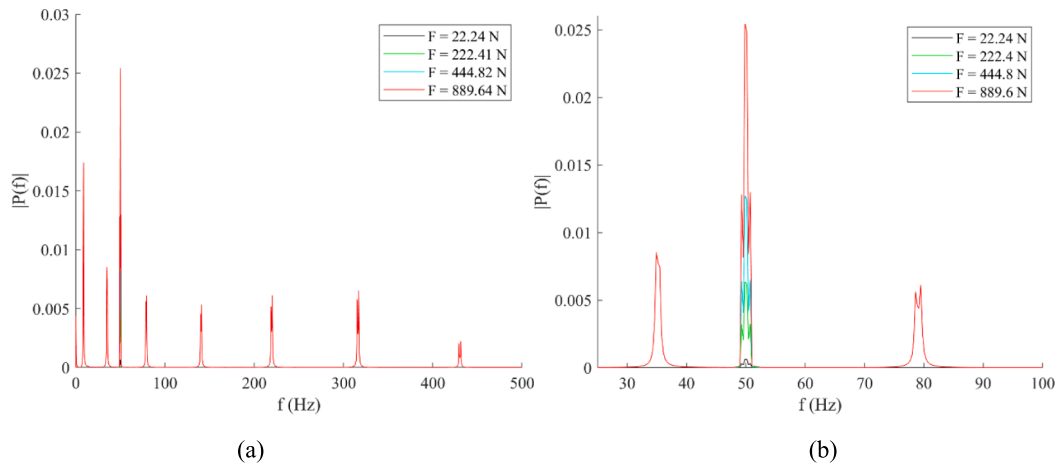

Fig. 3. Fourier spectra of vehicle acceleration signals under various excitation forces: (a) 0–500 Hz for multiple natural frequencies and (b) 25–100 Hz for a close-up view of the effect of peak force.

magnitude at the identified excitation frequency of 49.86 Hz (0.29% error) is 0.0636, which is approximately 3.66 times of the highest spectral value at the fundamental bridge frequency of 0.0174. Therefore, the vehicle self-generated excitation frequency may dominate the frequency spectrum and influence the extraction of bridge frequencies.

To study the effects of peak force and excitation frequency, two scenarios are considered here: (1) the peak force of vehicle excitation is set to $F = 22.24$ N, 222.4 N, 444.8 N, and 889.6 N corresponding to 1%, 10%, 20%, and 40% of the total engine weight, respectively, while an excitation frequency of 50 Hz is used; (2) the frequency of vehicle excitation is set to $\omega = 5$ Hz, 50 Hz, 100 Hz, and 200 Hz, while a peak force of F = 2,224 N is used. Figs. 3 and 4 present the Fourier transform of the vehicle acceleration signals under various peak forces and excitation frequencies, respectively. It can be seen from Fig. 3(b) that the magnitude at the excitation frequency approximately linearly increases from 6.380×10^{-4} through 6.360×10^{-3} and 1.272×10^{-2} to 2.543×10^{-2} as the peak force increases. When the peak force is too large, the pulse at the excitation frequency could dominate the spectrum and complicate the demarcation of the bridge frequencies. In application, a test vehicle must be designed to minimize its self-generated excitation. Notably in Fig. 4, as the excitation frequency increases from 5 Hz through 50 and 100 to 200 Hz, the spectral magnitude increases from

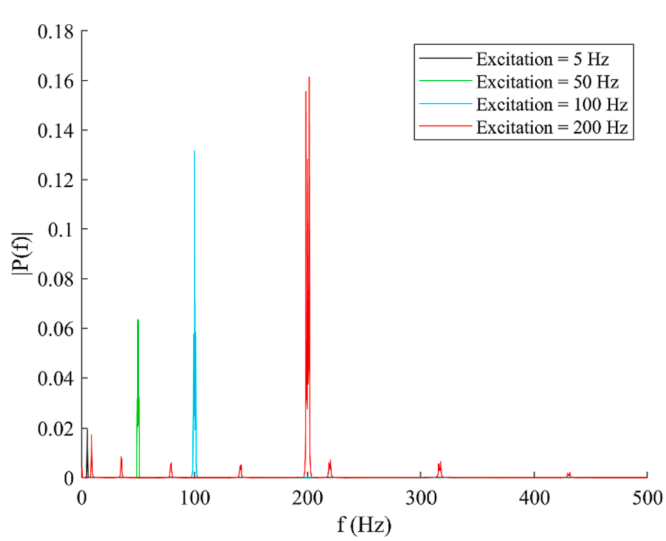

Fig. 4. Overshadowing effect of excitation frequency on the determination of bridge natural frequencies derived from a vehicle response under various excitation frequencies.

0.0195 through 0.0636 and 0.1317 to 0.1616, which have all exceeded the highest spectral value (0.0174) of the fundamental bridge frequency. In this case, the frequency of vehicle self-generated excitation must be identified before the bridge frequencies of interest can be reliably determined.

3.3. Contact point response

The maximum natural frequency that can be accurately identified from the bridge depends on the minimum time step that is closely related to the vehicle speed and the contact patch length. Fig. 5(a-c) presents the contact point responses and Fourier spectra when different contact patch lengths are considered. Note that the contact patch lengths chosen here are only intended to highlight its effect and shed lights on designing special vehicle bridge interaction systems. Different contact patch lengths may be achieved by changing wheel materials and/or configurations. The maximum frequency identifiable from the contact point responses decreases from 704 Hz through 176 Hz to 44 Hz as the contact patch length increases from ¼ in. (6.35×10^{-3} m) through 1 in. (0.0254 m) to 4 in. (0.1016 m). The number of distinguishable points along the bridge also decreases from 4800 through 1200 to 300.

An increase of vehicle speed from 20 mph (8.941 $\mathrm{m{\cdot}s^{-1}}$) in Fig. 5(b) to 80 mph (35.76 $\mathrm{m{\cdot}s^{-1}}$) in Fig. 5(d) does not reduce the maximum identifiable frequency 176 Hz but introduces more peak-splitting in the Fourier spectrum and thus more uncertain in identifying the natural frequencies due to the amplified camel hump phenomenon. At the same time, the signal strength increases from 0.1082 $\mathrm{m{\cdot}s^{-2}}$ in Fig. 5(a) to 0.6061 $\mathrm{m{\cdot}s^{-2}}$ in Fig. 5(d) and the signal length in time is shortened from 3.41 s in Fig. 5(a-c) to 0.85 s in Fig. 5(d). Both increasing the vehicle speed and/or decreasing the contact patch length in the form of $v/(2L_c)$ can increase the maximum identifiable frequency from the contact point signals. The increased signal magnitude and prominent camel hump phenomenon could challenge the validity of $\ddot{y}_v \ll g$ and the extraction of bridge frequencies due to increased noise effects.

3.4. Mode shape and damping ratio extraction

The extraction of bridge mode shapes and damping ratios are illustrated in this subsection. The ratio of $n\pi v/L$ to ω_{nd} based on the selected parameters in Table 1 are 1.67%, 0.83%, 0.56%, 0.42%, and 0.33% for the first five modes of bridge vibration, respectively. Therefore, the assumption of $n\pi v/L \ll \omega_{nd}$ is reasonable. Fig. 6 shows the displacement and acceleration signals from the vehicle and their Fourier spectra. Although multiple bridge frequencies could be identified, the magnitude from the displacement signal is much weaker and significantly drops for

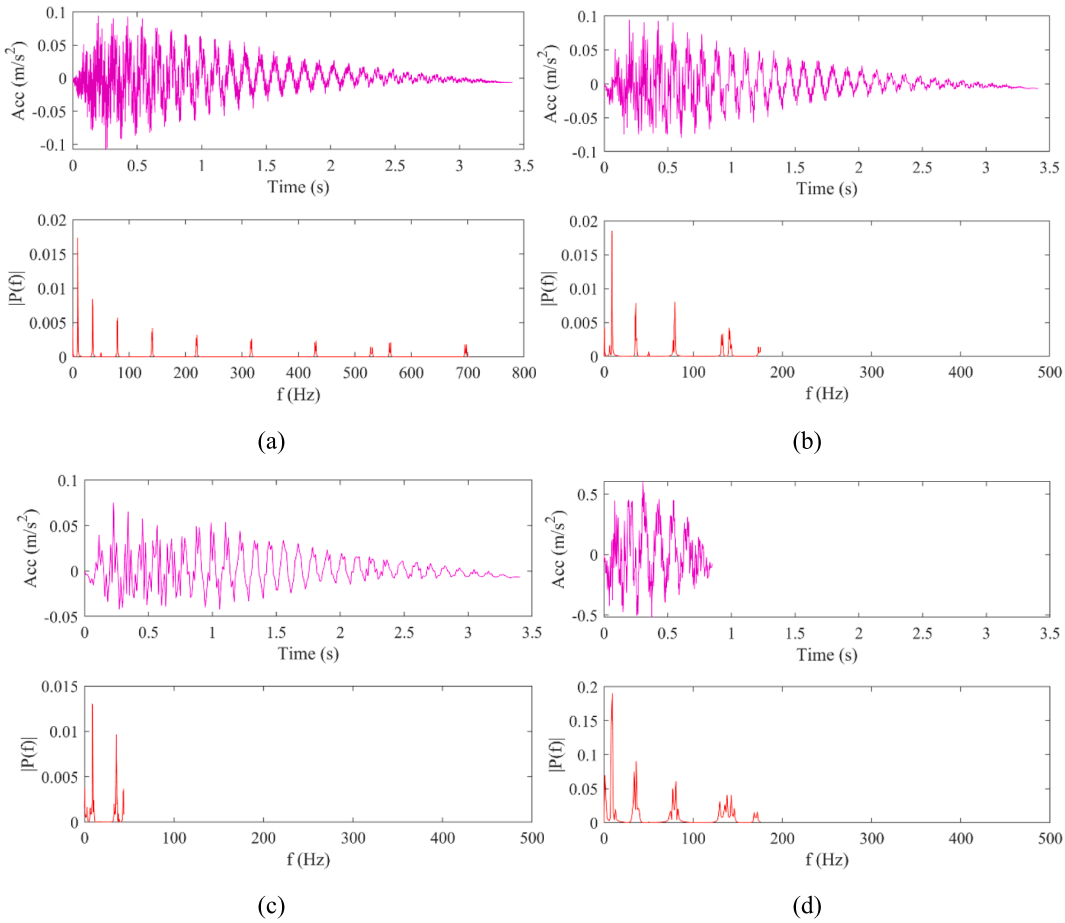

Fig. 5. Maximum frequency identifiable from contact point responses: (a) 704 Hz with a contact patch length of ¼ in (6.35×10^{-3} m), (b) 176 Hz with a contact patch length of 1 in (0.0254 m), (c) 44 Hz with a contact patch length of 4 in (0.1016 m), and (d) 176 Hz when the vehicle speed is increased by four times of the benchmark value.

the second and higher modes. Mode 2 and higher modes contribute much less toward the total displacement signal. The magnitude of mode 2 (1.7723×10^{-7}) is only 3.11% of that of mode 1 (5.6912×10^{-6}). On the contrary, the acceleration signal is more suitable for multiple mode shapes and damping ratios extraction, as the acceleration magnitude of mode 5 (6.114×10^{-3}) is still 35% of that of the mode 1 (1.739×10^{-2}).

Fig. 7 shows the Hilbert Transform of the decomposed signal for each bridge vibration mode, in which both the real and imaginary parts are plotted. Fig. 8 presents the instantaneous amplitudes of the Hilbert-Transformed signals. The instantaneous amplitude of the transformed signal contains the absolute value of bridge mode shape as expressed in Eq. (26) and Eq. (27). The overall decreasing peaks are caused by the damping effect. Note that this procedure works only after each bridge frequency has been identified. For the determination of each mode

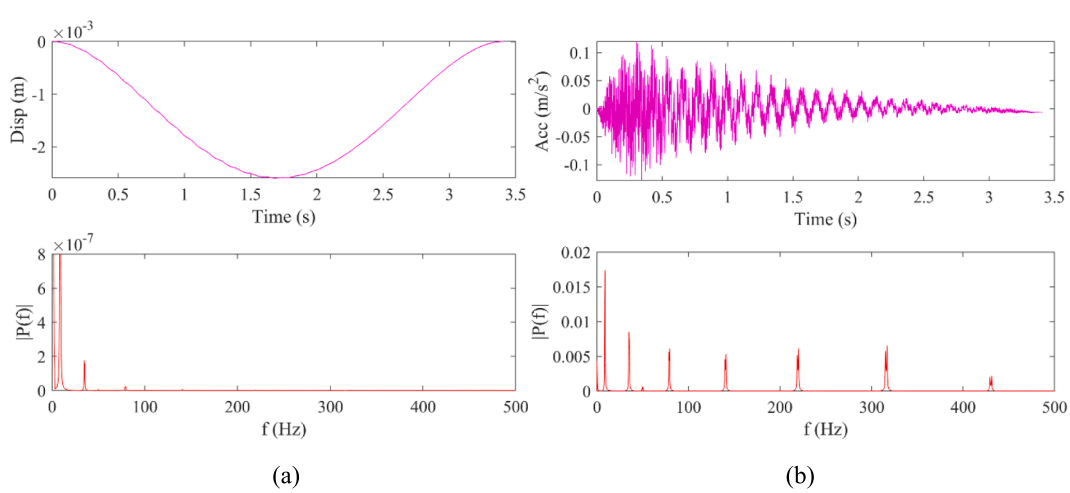

Fig. 6. Vehicle signal and its Fourier spectrum: (a) Displacement and (b) Acceleration.

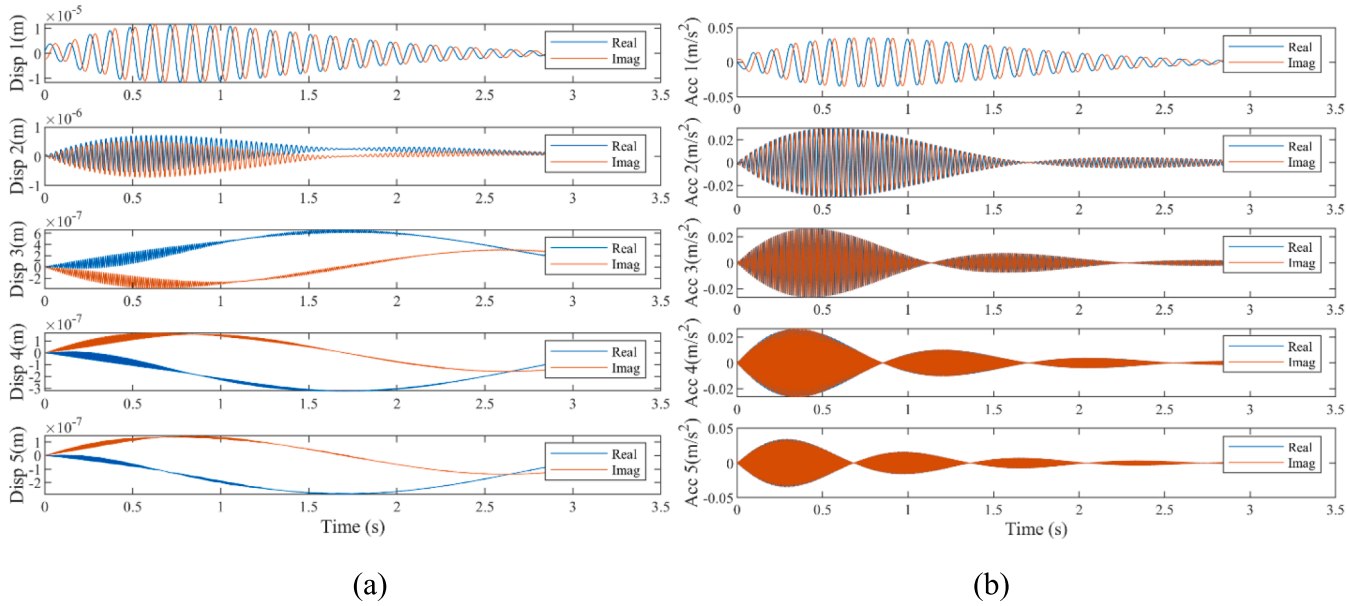

Fig. 7. Hilbert Transforms of decomposed signals corresponding to the first five natural frequencies of the bridge: (a) Displacement and (b) Acceleration.

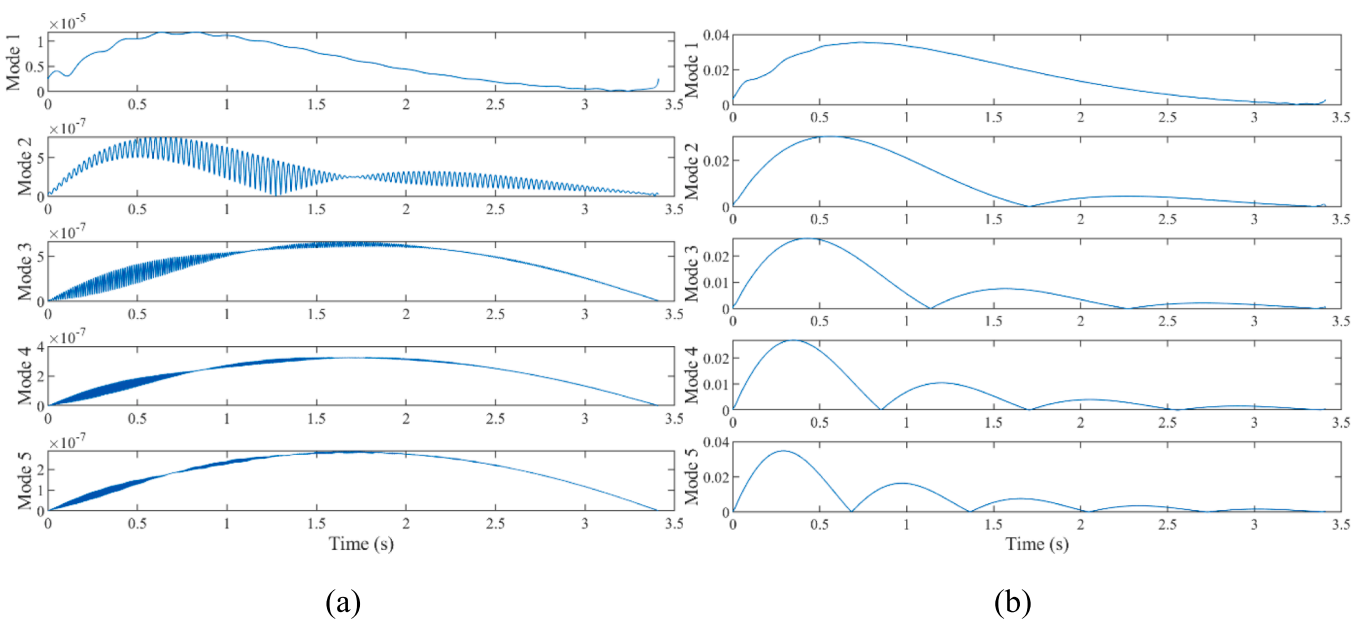

Fig. 8. Instantaneous amplitude from the Hilbert Transform of vehicle signals: (a) Displacement and (b) Acceleration.

Table 4
Bridge damping ratio extracted from the vehicle acceleration signal.

Mode	Theoretical	Instantaneous Amplitude	Error (%)
1	2.000×10^{-2}	2.008×10^{-2}	0.41%
2	5.000×10^{-3}	4.991×10^{-3}	0.18%
3	2.222×10^{-4}	2.230×10^{-4}	0.37%
4	1.250×10^{-4}	1.255×10^{-4}	0.43%
5	8.000×10^{-4}	8.001×10^{-4}	0.01%

shape, the other modal responses and the responses associated with vehicle frequency and excitation frequency need to be filtered out before constructing the bridge mode shape.

The damping ratios can also be calculated from Eq. (28) and Eq. (29) based on the instantaneous acceleration amplitudes as shown in Fig. 8 (b). Table 4 compares the calculated damping ratios with the theoretical values from Eq. (4). Note that the first two peaks with their corresponding time instances are picked as two consecutive peaks in the calculation of second and higher modal damping ratios. Since there is only one peak for the first mode, the damping ratio is calculated using the instantaneous amplitude at the quarter and third-quarter time instances based on Eq. (29). The overall damping ratio identification shows an average error of 0.28%.

4. Conclusions

This paper proposes a coupled, single-axle vehicle bridge interaction model with the consideration of the wheel-bridge contact patch and the motor-induced vehicle excitation which would shed more lights on designing effective VBI system. The contact point responses are also derived for the first time both from the vehicle and bridge to confirm their equivalence. The estimation of the contact patch length essential to the maximum identifiable frequency, is then discussed for both

pneumatic tire and solid wheel scenarios. The interaction model accounts for multiple modal contributions in damped vibration of the bridge and the vehicle. When the vertical vehicle acceleration is significantly smaller than the gravitational acceleration constant, the equations of bridge and vehicle motions could be uncoupled, and their closed-form solutions could be formulated theoretically. The procedure to extract multiple mode shapes and damping ratios are also presented. Based on the analytical derivations and parametric studies, the following conclusions can be drawn:

1. The vehicle responses represent an average effect of the vehicle-bridge interaction over a contact patch length. Therefore, the minimum time in which the vehicle passes through the contact patch length at certain speed can be logically used to determine the maximum identifiable bridge frequency of interest and the maximum number of sampling points along the bridge.
2. In general, the higher elastic modulus of the wheel, the shorter contact patch length, and the higher maximum identifiable frequency. The contact patch length due to pneumatic tire is significantly larger than that due to solid wheel, which would significantly reduce the maximum identifiable frequency.
3. The presence of a vehicle excitation likely affects the extractability of multiple bridge frequencies from the vehicle responses. The stronger the vehicle excitation, the more dominant the excitation frequency over other frequency components. Thus, the vehicle self-generated excitation should not be overlooked in the VBI system.
4. The vehicle acceleration response is more effective than the vehicle displacement response in extracting the mode shapes and damping ratios of a bridge as the acceleration includes more modal contributions from higher vibration modes of the bridge.
5. Multiple damping ratios extracted from the instantaneous amplitude of Hilbert Transformed responses show an average error of 0.28% and a maximum error of less than 0.5%.
6. The contact point responses (both displacement and acceleration) are derived both from the vehicle and bridge responses and confirmed equivalent; they exclude the vehicle frequency component which may otherwise overshadow the analysis of the bridge frequencies.

CRediT authorship contribution statement

Zhenhua Shi: Conceptualization, Data curation, Formal analysis, Investigation, Methodology, Resources, Validation, Visualization, Writing – original draft, Writing – review & editing. **Yahya M. Mohammed:** Conceptualization, Methodology, Resources, Writing – review & editing. **Nasim Uddin:** Conceptualization, Methodology, Resources, Project administration, Supervision, Writing – review & editing. **Genda Chen:** Conceptualization, Formal analysis, Funding acquisition, Investigation, Methodology, Project administration, Resources, Supervision, Validation, Visualization, Writing – review & editing.

Declaration of Competing Interest

The authors declare that they have no known competing financial interests or personal relationships that could have appeared to influence the work reported in this paper.

Data availability

Data will be made available on request.

Acknowledgement

Financial support to complete this study was provided in part by the National Science Foundation [grant numbers NSF-CNS-1645863, NSF-CSR-1813949], and by the Transportation Pooled Fund Program under Project No. TPF-5(395). Additional resources provided by the INSPIRE University Transportation Center and the Center for Intelligent Infrastructure at Missouri University of Science and Technology are also appreciated. The views, opinions, and conclusions reflected in this paper are solely those of the authors and do not represent the official policy or position of the sponsors.

Appendices

Appendix A

$$\begin{cases} Q_n = -(S_{n1} + S_{n2} + S_{n3}) \\ R_n = -\dfrac{\xi_n \omega_n (S_{n1} + S_{n2} + S_{n3}) + \dfrac{n\pi v}{L}\left(T_{n1} - \alpha_{n\omega}^{-} T_{n2} + \alpha_{n\omega}^{+} T_{n3}\right)}{\omega_{nd}} \end{cases} \tag{A.1}$$

$$\begin{cases} S_{n1} = \dfrac{2p_n m_v g}{mL} \dfrac{2\xi_n \omega_n \dfrac{n\pi v}{L}}{\left[\omega_n^2 - \left(\dfrac{n\pi v}{L}\right)^2\right]^2 + \left(2\xi_n \omega_n \dfrac{n\pi v}{L}\right)^2} \\ T_{n1} = -\dfrac{2p_n m_v g}{mL} \dfrac{\left[\omega_n^2 - \left(\dfrac{n\pi v}{L}\right)^2\right]}{\left[\omega_n^2 - \left(\dfrac{n\pi v}{L}\right)^2\right]^2 + \left(2\xi_n \omega_n \dfrac{n\pi v}{L}\right)^2} \end{cases} \tag{A.2}$$

$$\begin{cases} S_{n2} = \dfrac{p_n F}{mL} \dfrac{\left[\omega_n^2 - \left(\alpha_{n\omega}^- \dfrac{n\pi v}{L}\right)^2\right]}{\left[\omega_n^2 - \left(\alpha_{n\omega}^- \dfrac{n\pi v}{L}\right)^2\right]^2 + \left(2\xi_n \omega_n \alpha_{n\omega}^- \dfrac{n\pi v}{L}\right)^2} \\ T_{n2} = -\dfrac{p_n F}{mL} \dfrac{2\xi_n \omega_n \alpha_{n\omega}^- \dfrac{n\pi v}{L}}{\left[\omega_n^2 - \left(\alpha_{n\omega}^- \dfrac{n\pi v}{L}\right)^2\right]^2 + \left(2\xi_n \omega_n \alpha_{n\omega}^- \dfrac{n\pi v}{L}\right)^2} \end{cases} \tag{A.3}$$

$$\begin{cases} S_{n3} = -\dfrac{p_n F}{mL} \dfrac{\left[\omega_n^2 - \left(\alpha_{n\omega}^+ \dfrac{n\pi v}{L}\right)^2\right]}{\left[\omega_n^2 - \left(\alpha_{n\omega}^+ \dfrac{n\pi v}{L}\right)^2\right]^2 + \left(2\xi_n \omega_n \alpha_{n\omega}^+ \dfrac{n\pi v}{L}\right)^2} \\ T_{n3} = -\dfrac{p_n F}{mL} \dfrac{2\xi_n \omega_n \alpha_{n\omega}^+ \dfrac{n\pi v}{L}}{\left[\omega_n^2 - \left(\alpha_{n\omega}^+ \dfrac{n\pi v}{L}\right)^2\right]^2 + \left(2\xi_n \omega_n \alpha_{n\omega}^+ \dfrac{n\pi v}{L}\right)^2} \end{cases} \tag{A.4}$$

Appendix B

$$\begin{cases} U_1 = A_1 + \dfrac{1}{2}\sum_n M_{n2}, \quad V_1 = B_1 + \dfrac{1}{2}\sum_n N_{n2} \\ U_2 = C_1 + \dfrac{1}{2}\sum_n M_{n6}, \quad V_2 = D_1 + \dfrac{1}{2}\sum_n N_{n6} \\ M_{n2} = A_{n2} + \cdots + A_{n14}, \quad N_{n2} = B_{n2} + \cdots + B_{n14} \\ M_{n3} = C_{n2} + C_{n5}, \quad N_{n3} = D_{n2} + D_{n5} \\ M_{n4} = C_{n3} + C_{n4}, \quad N_{n4} = D_{n3} + D_{n4} \\ M_{n5} = C_{n6} + C_{n10}, \quad N_{n5} = D_{n6} + D_{n10} \\ M_{n6} = C_{n7} + C_{n11}, \quad N_{n6} = D_{n7} + D_{n11} \\ M_{n7} = C_{n8} + C_{n12}, \quad N_{n7} = D_{n8} + D_{n12} \\ M_{n8} = C_{n9} + C_{n13}, \quad N_{n8} = D_{n9} + D_{n13} \end{cases} \tag{B.1}$$

$$\begin{cases} A_1 = -C_1 \\ B_1 = -\dfrac{\xi_v \omega_v C_1 + \omega D_1}{\omega_{vd}} \\ C_1 = -\dfrac{F}{m_v} \dfrac{2\xi_v \omega_v \omega}{\left(\omega_v^2 - \omega^2\right)^2 + \left(2\xi_v \omega_v \omega\right)^2} \\ D_1 = \dfrac{F}{m_v} \dfrac{\omega_v^2 - \omega^2}{\left(\omega_v^2 - \omega^2\right)^2 + \left(2\xi_v \omega_v \omega\right)^2} \end{cases} \tag{B.2}$$

$$\begin{cases} A_{n2} = -C_{n2} \\ B_{n2} = \dfrac{-\xi_v\omega_v C_{n2} + \xi_n\omega_n C_{n2} + \beta^-_{n\omega_{nd}}\dfrac{n\pi v}{L}D_{n2}}{\omega_{vd}} \\ C_{n2} = b^*_n \dfrac{(\xi_n\omega_n)^2 - \left(\beta^-_{n\omega_{nd}}\dfrac{n\pi v}{L}\right)^2 - 2\xi_v\omega_v\xi_n\omega_n + \omega_v^2}{\left[(\xi_n\omega_n)^2 - \left(\beta^-_{n\omega_{nd}}\dfrac{n\pi v}{L}\right)^2 - 2\xi_v\omega_v\xi_n\omega_n + \omega_v^2\right]^2 + \left[2\beta^-_{n\omega_{nd}}\dfrac{n\pi v}{L}(\xi_n\omega_n - \xi_v\omega_v)\right]^2} \\ D_{n2} = b^*_n \dfrac{2(\xi_n\omega_n - \xi_v\omega_v)\beta^-_{n\omega_{nd}}\dfrac{n\pi v}{L}}{\left[(\xi_n\omega_n)^2 - \left(\beta^-_{n\omega_{nd}}\dfrac{n\pi v}{L}\right)^2 - 2\xi_v\omega_v\xi_n\omega_n + \omega_v^2\right]^2 + \left[2\beta^-_{n\omega_{nd}}\dfrac{n\pi v}{L}(\xi_n\omega_n - \xi_v\omega_v)\right]^2} \end{cases} \tag{B.3}$$

$$\begin{cases} A_{n3} = -C_{n3} \\ B_{n3} = \dfrac{-\xi_v\omega_v C_{n3} + \xi_n\omega_n C_{n3} - \beta^+_{n\omega_{nd}}\dfrac{n\pi v}{L}D_{n3}}{\omega_{vd}} \\ C_{n3} = -b^*_n \dfrac{(\xi_n\omega_n)^2 - \left(\beta^+_{n\omega_{nd}}\dfrac{n\pi v}{L}\right)^2 - 2\xi_v\omega_v\xi_n\omega_n + \omega_v^2}{\left[(\xi_n\omega_n)^2 - \left(\beta^+_{n\omega_{nd}}\dfrac{n\pi v}{L}\right)^2 - 2\xi_v\omega_v\xi_n\omega_n + \omega_v^2\right]^2 + \left[2\left(\beta^+_{n\omega_{nd}}\dfrac{n\pi v}{L}\right)(\xi_n\omega_n - \xi_v\omega_v)\right]^2} \\ D_{n3} = b^*_n \dfrac{2(\xi_n\omega_n - \xi_v\omega_v)\beta^+_{n\omega_{nd}}\dfrac{n\pi v}{L}}{\left[(\xi_n\omega_n)^2 - \left(\beta^+_{n\omega_{nd}}\dfrac{n\pi v}{L}\right)^2 - 2\xi_v\omega_v\xi_n\omega_n + \omega_v^2\right]^2 + \left[2\left(\beta^+_{n\omega_{nd}}\dfrac{n\pi v}{L}\right)(\xi_n\omega_n - \xi_v\omega_v)\right]^2} \end{cases} \tag{B.4}$$

$$\begin{cases} A_{n4} = -C_{n4} \\ B_{n4} = \dfrac{-\xi_v\omega_v C_{n4} + \xi_n\omega_n C_{n4} - \beta^+_{n\omega_{nd}}\dfrac{n\pi v}{L}D_{n4}}{\omega_{vd}} \\ C_{n4} = a^*_n \dfrac{2(\xi_n\omega_n - \xi_v\omega_v)\beta^+_{n\omega_{nd}}\dfrac{n\pi v}{L}}{\left[(\xi_n\omega_n)^2 - \left(\beta^+_{n\omega_{nd}}\dfrac{n\pi v}{L}\right)^2 - 2\xi_v\omega_v\xi_n\omega_n + \omega_v^2\right]^2 + \left[2\beta^+_{n\omega_{nd}}\dfrac{n\pi v}{L}(\xi_n\omega_n - \xi_v\omega_v)\right]^2} \\ D_{n4} = a^*_n \dfrac{(\xi_n\omega_n)^2 - \left(\beta^+_{n\omega_{nd}}\dfrac{n\pi v}{L}\right)^2 - 2\xi_v\omega_v\xi_n\omega_n + \omega_v^2}{\left[(\xi_n\omega_n)^2 - \left(\beta^+_{n\omega_{nd}}\dfrac{n\pi v}{L}\right)^2 - 2\xi_v\omega_v\xi_n\omega_n + \omega_v^2\right]^2 + \left[2\beta^+_{n\omega_{nd}}\dfrac{n\pi v}{L}(\xi_n\omega_n - \xi_v\omega_v)\right]^2} \end{cases} \tag{B.5}$$

$$\begin{cases} A_{n5} = -C_{n5} \\ B_{n5} = \dfrac{-\xi_v\omega_v C_{n5} + \xi_n\omega_n C_{n5} + \beta^-_{n\omega_{nd}}\dfrac{n\pi v}{L}D_{n5}}{\omega_{vd}} \\ C_{n5} = a^*_n \dfrac{2(\xi_n\omega_n - \xi_v\omega_v)\beta^-_{n\omega_{nd}}\dfrac{n\pi v}{L}}{\left[(\xi_n\omega_n)^2 - \left(\beta^-_{n\omega_{nd}}\dfrac{n\pi v}{L}\right)^2 - 2\xi_v\omega_v\xi_n\omega_n + \omega_v^2\right]^2 + \left[2\beta^-_{n\omega_{nd}}\dfrac{n\pi v}{L}(\xi_n\omega_n - \xi_v\omega_v)\right]^2} \\ D_{n5} = -a^*_n \dfrac{(\xi_n\omega_n)^2 - \left(\beta^-_{n\omega_{nd}}\dfrac{n\pi v}{L}\right)^2 - 2\xi_v\omega_v\xi_n\omega_n + \omega_v^2}{\left[(\xi_n\omega_n)^2 - \left(\beta^-_{n\omega_{nd}}\dfrac{n\pi v}{L}\right)^2 - 2\xi_v\omega_v\xi_n\omega_n + \omega_v^2\right]^2 + \left[2\beta^-_{n\omega_{nd}}\dfrac{n\pi v}{L}(\xi_n\omega_n - \xi_v\omega_v)\right]^2} \end{cases} \tag{B.6}$$

$$\begin{cases} A_{n6} = -C_{n6} \\ B_{n6} = -\dfrac{\xi_v \omega_v C_{n6} + \dfrac{2n\pi v}{L} D_{n6}}{\omega_{vd}} \\ C_{n6} = -d_n^* \dfrac{\omega_v^2 - \left(\dfrac{2n\pi v}{L}\right)^2}{\left[\omega_v^2 - \left(\dfrac{2n\pi v}{L}\right)^2\right]^2 + \left(2\xi_v \omega_v \dfrac{2n\pi v}{L}\right)^2} \\ D_{n6} = -d_n^* \dfrac{2\xi_v \omega_v \dfrac{2n\pi v}{L}}{\left[\omega_v^2 - \left(\dfrac{2n\pi v}{L}\right)^2\right]^2 + \left(2\xi_v \omega_v \dfrac{2n\pi v}{L}\right)^2} \end{cases} \tag{B.7}$$

$$\begin{cases} A_{n7} = -C_{n7} \\ B_{n7} = -\dfrac{\xi_v \omega_v C_{n7} + \omega D_{n7}}{\omega_{vd}} \\ C_{n7} = \left(h_n^* - f_n^*\right) \dfrac{\omega_v^2 - \omega^2}{\left(\omega_v^2 - \omega^2\right)^2 + \left(2\xi_v \omega_v \omega\right)^2} \\ D_{n7} = \left(h_n^* - f_n^*\right) \dfrac{2\xi_v \omega_v \omega}{\left(\omega_v^2 - \omega^2\right)^2 + \left(2\xi_v \omega_v \omega\right)^2} \end{cases} \tag{B.8}$$

$$\begin{cases} A_{n8} = -C_{n8} \\ B_{n8} = -\dfrac{\xi_v \omega_v C_{n8} - \alpha_{2n\omega}^- \dfrac{2n\pi v}{L} D_{n8}}{\omega_{vd}} \\ C_{n8} = f_n^* \dfrac{\omega_v^2 - \left(\alpha_{2n\omega}^- \dfrac{2n\pi v}{L}\right)^2}{\left[\omega_v^2 - \left(\alpha_{2n\omega}^- \dfrac{2n\pi v}{L}\right)^2\right]^2 + \left(2\xi_v \omega_v \alpha_{2n\omega}^- \dfrac{2n\pi v}{L}\right)^2} \\ D_{n8} = -f_n^* \dfrac{2\xi_v \omega_v \alpha_{2n\omega}^- \dfrac{2n\pi v}{L}}{\left[\omega_v^2 - \left(\alpha_{2n\omega}^- \dfrac{2n\pi v}{L}\right)^2\right]^2 + \left(2\xi_v \omega_v \alpha_{2n\omega}^- \dfrac{2n\pi v}{L}\right)^2} \end{cases} \tag{B.9}$$

$$\begin{cases} A_{n9} = -C_{n9} \\ B_{n9} = -\dfrac{\xi_v \omega_v C_{n9} + \alpha_{2n\omega}^+ \dfrac{2n\pi v}{L} D_{n9}}{\omega_{vd}} \\ C_{n9} = -h_n^* \dfrac{\omega_v^2 - \left(\alpha_{2n\omega}^+ \dfrac{2n\pi v}{L}\right)^2}{\left[\omega_v^2 - \left(\alpha_{2n\omega}^+ \dfrac{2n\pi v}{L}\right)^2\right]^2 + \left(2\xi_v \omega_v \alpha_{2n\omega}^+ \dfrac{2n\pi v}{L}\right)^2} \\ D_{n9} = -h_n^* \dfrac{2\xi_v \omega_v \left(\alpha_{2n\omega}^+ \dfrac{2n\pi v}{L}\right)}{\left[\omega_v^2 - \left(\alpha_{2n\omega}^+ \dfrac{2n\pi v}{L}\right)^2\right]^2 + \left(2\xi_v \omega_v \alpha_{2n\omega}^+ \dfrac{2n\pi v}{L}\right)^2} \end{cases} \tag{B.10}$$

$$\begin{cases} A_{n10} = -C_{n10} \\ B_{n10} = -\dfrac{\xi_v\omega_v C_{n10} + \dfrac{2n\pi v}{L} D_{n10}}{\omega_{vd}} \\ C_{n10} = -c_n^* \dfrac{2\xi_v\omega_v \dfrac{2n\pi v}{L}}{\left[\omega_v^2 - \left(\dfrac{2n\pi v}{L}\right)^2\right]^2 + \left(2\xi_v\omega_v \dfrac{2n\pi v}{L}\right)^2} \\ D_{n10} = c_n^* \dfrac{\omega_v^2 - \left(\dfrac{2n\pi v}{L}\right)^2}{\left[\omega_v^2 - \left(\dfrac{2n\pi v}{L}\right)^2\right]^2 + \left(2\xi_v\omega_v \dfrac{2n\pi v}{L}\right)^2} \end{cases} \tag{B.11}$$

$$\begin{cases} A_{n11} = -C_{n11} \\ B_{n11} = -\dfrac{\xi_v\omega_v C_{n11} + \omega D_{n11}}{\omega_{vd}} \\ C_{n11} = -\left(e_n^* - g_n^*\right) \dfrac{2\xi_v\omega_v\omega}{\left(\omega_v^2 - \omega^2\right)^2 + \left(2\xi_v\omega_v\omega\right)^2} \\ D_{n11} = \left(e_n^* - g_n^*\right) \dfrac{\omega_v^2 - \omega^2}{\left(\omega_v^2 - \omega^2\right)^2 + \left(2\xi_v\omega_v\omega\right)^2} \end{cases} \tag{B.12}$$

$$\begin{cases} A_{n12} = -C_{n12} \\ B_{n12} = -\dfrac{\xi_v\omega_v C_{n12} - \alpha_{2n\omega}^- \dfrac{2n\pi v}{L} D_{n12}}{\omega_{vd}} \\ C_{n12} = -e_n^* \dfrac{2\xi_v\omega_v\alpha_{2n\omega}^- \dfrac{2n\pi v}{L}}{\left[\omega_v^2 - \left(\alpha_{2n\omega}^- \dfrac{2n\pi v}{L}\right)^2\right]^2 + \left(2\xi_v\omega_v\alpha_{2n\omega}^- \dfrac{2n\pi v}{L}\right)^2} \\ D_{n12} = -e_n^* \dfrac{\omega_v^2 - \left(\alpha_{2n\omega}^- \dfrac{2n\pi v}{L}\right)^2}{\left[\omega_v^2 - \left(\alpha_{2n\omega}^- \dfrac{2n\pi v}{L}\right)^2\right]^2 + \left(2\xi_v\omega_v\alpha_{2n\omega}^- \dfrac{2n\pi v}{L}\right)^2} \end{cases} \tag{B.13}$$

$$\begin{cases} A_{n13} = -C_{n13} \\ B_{n13} = -\dfrac{\xi_v\omega_v C_{n13} + \alpha_{2n\omega}^+ \dfrac{2n\pi v}{L} D_{n13}}{\omega_{vd}} \\ C_{n13} = -g_n^* \dfrac{2\xi_v\omega_v\alpha_{2n\omega}^+ \dfrac{2n\pi v}{L}}{\left[\omega_v^2 - \left(\alpha_{2n\omega}^+ \dfrac{2n\pi v}{L}\right)^2\right]^2 + \left(2\xi_v\omega_v\alpha_{2n\omega}^+ \dfrac{2n\pi v}{L}\right)^2} \\ D_{n13} = g_n^* \dfrac{\omega_v^2 - \left(\alpha_{2n\omega}^+ \dfrac{2n\pi v}{L}\right)^2}{\left[\omega_v^2 - \left(\alpha_{2n\omega}^+ \dfrac{2n\pi v}{L}\right)^2\right]^2 + \left(2\xi_v\omega_v\alpha_{2n\omega}^+ \dfrac{2n\pi v}{L}\right)^2} \end{cases} \tag{B.14}$$

$$\begin{cases} A_{n14} = -\dfrac{d_n^*}{\omega_v^2} \\ B_{n14} = \dfrac{\xi_v}{\sqrt{1-\xi_v^2}} A_{14} \end{cases} \tag{B.15}$$

References

[1] Yang YB, Lin CW, Yau JD. Extracting bridge frequencies from the dynamic response of a passing vehicle. J Sound Vib 2004;272(3–5):471–93. https://doi.org/10.1016/s0022-460x(03)00378-x.

[2] Lin CW, Yang YB. Use of a passing vehicle to scan the fundamental bridge frequencies: An experimental verification. Eng Struct 2005;27(13):1865–78. https://doi.org/10.1016/j.engstruct.2005.06.016.

[3] Yang YB, Chang KC. Extraction of bridge frequencies from the dynamic response of a passing vehicle enhanced by the EMD technique. J Sound Vib 2009;322(4–5): 718–39. https://doi.org/10.1016/j.jsv.2008.11.028.

[4] Yang YB, Chang KC. Extracting the bridge frequencies indirectly from a passing vehicle: Parametric study. Eng Struct 2009;31(10):2448–59. https://doi.org/10.1016/j.engstruct.2009.06.001.

[5] Yang YB, Chen WF, Yu HW, Chan CS. Experimental study of a hand-drawn cart for measuring the bridge. Eng Struct 2013;57:222–31. https://doi.org/10.1016/j.engstruct.2013.09.007.

[6] Yang YB, Chen WF. Extraction of bridge frequencies from a moving test vehicle by stochastic subspace identification. J Bridg Eng 2016;21(3):04015053. https://doi.org/10.1061/(asce)be.1943-5592.0000792.

[7] Xu H, Huang CC, Wang ZL, Shi K, Wu YT, Yang YB. Damped test vehicle for scanning bridge frequencies: Theory, simulation and experiment. J Sound Vib 2021;506:116155. https://doi.org/10.1016/j.jsv.2021.116155.

[8] Yang YB, Xu H, Wang ZL, Shi K, Wu YT. Refined detection technique for bridge frequencies using rocking motion of single-axle moving vehicle. Mech Syst Sig Process 2022;162:107992. https://doi.org/10.1016/j.ymssp.2021.107992.

[9] Yang YB, Li Z, Wang ZL, Shi K, Xu H, Qiu FQ, et al. A novel frequency-free movable test vehicle for retrieving modal parameters of bridges: Theory and experiment. Mech Syst Sig Process 2022;170:108854. https://doi.org/10.1016/j.ymssp.2022.108854.

[10] Yang JP, Cao C-Y. Wheel size embedded two-mass vehicle model for scanning bridge frequencies. Acta Mech 2020;231(4):1461–75. https://doi.org/10.1007/s00707-019-02595-5.

[11] Yang JP, Feng T-Y. Enhancing a three-mass vehicle model with wheel-size effect for scanning bridge frequencies. Int J Appl Mech 2023;15(07). https://doi.org/10.1142/s1758825123500564.

[12] Yang YB, Li YC, Chang KC. Constructing the mode shapes of a bridge from a passing vehicle: a theoretical study. Smart Struct Syst 2014;13(5):797–819. https://doi.org/10.12989/sss.2014.13.5.797.

[13] Malekjafarian A, OBrien EJ. Identification of bridge mode shapes using short time frequency domain decomposition of the responses measured in a passing vehicle. Eng Struct 2014;81:386–97. https://doi.org/10.1016/j.engstruct.2014.10.007.

[14] OBrien EJ, Malekjafarian A. A mode shape-based damage detection approach using laser measurement from a vehicle crossing a simply supported bridge. Struct Control Health Monit 2016;23(10):1273–86. https://doi.org/10.1002/stc.1841.

[15] Malekjafarian A, OBrien EJ. On the use of a passing vehicle for the estimation of bridge mode shapes. J Sound Vib 2017;397:77–91. https://doi.org/10.1016/j.jsv.2017.02.051.

[16] Oshima Y, Yamamoto K, Sugiura K. Damage assessment of a bridge based on mode shapes estimated by responses of passing vehicles. Smart Struct Syst 2014;13(5): 731–53. https://doi:10.12989/sss.2014.13.5.731.

[17] Qi ZQ, Au FTK. Identifying mode shapes of girder bridges using dynamic responses extracted from a moving vehicle under impact excitation. Int J Struct Stab Dyn 2017;17(08):1750081. https://doi.org/10.1142/s021945541750081x.

[18] He WY, Ren WX, Zuo XH. Mass-normalized mode shape identification method for bridge structures using parking vehicle-induced frequency change. Struct Control Health Monit 2018;25(6):e2174. https://doi:10.1002/stc.2174.

[19] Nayek R, Mukhopadhyay S, Narasimhan S. Mass normalized mode shape identification of bridge structures using a single actuator-sensor pair. Struct Control Health Monit 2018;25(11):e2244. https://doi:10.1002/stc.2244.

[20] Zhang Y, Wang L, Zhao H, Lie ST. Extraction of mode shapes of beam-like structures from the dynamic response of a moving mass. Acta Mech Sin 2019;35(3): 664–73. https://doi:10.1007/s10409-018-0831-7.

[21] Zhang Y, Zhao H, Lie ST. Estimation of mode shapes of beam-like structures by a moving lumped mass. Eng Struct 2019;180:654–68. https://doi:10.1016/j.engstruct.2018.11.074.

[22] He Y, Yang JP, Chen J. Estimating bridge modal parameters from residual response of two-connected vehicles. J Vib Eng Technol 2022. https://doi.org/10.1007/s42417-022-00724-4.

[23] He Y, Yang JP, Yan Z. Enhanced identification of bridge modal parameters using contact residuals from three-connected vehicles: Theoretical study. Structures 2023;54:1320–35. https://doi.org/10.1016/j.istruc.2023.05.112.

[24] González A, OBrien EJ, McGetrick PJ. Identification of damping in a bridge using a moving instrumented vehicle. J Sound Vib 2012;331(18):4115–31. https://doi.org/10.1016/j.jsv.2012.04.019.

[25] Keenahan J, OBrien EJ, McGetrick PJ, Gonzalez A. The use of a dynamic truck–trailer drive-by system to monitor bridge damping. Struct Health Monit 2014;13(2):143–57. https://doi.org/10.1177/1475921713513974.

[26] Yang YB, Zhang B, Chen Y, Qian Y, Wu Y. Bridge damping identification by vehicle scanning method. Eng Struct 2019;183:637–45.

[27] Yang YB, Zhang B, Qian Y, Wu Y. Contact-Point Response for Modal Identification of Bridges by a Moving Test Vehicle. Int J Struct Stab Dyn 2018;18(05):1850073. https://doi.org/10.1142/s0219455418500736.

[28] Yang YB, Xu H, Wang ZL, Shi K. Using vehicle–bridge contact spectra and residue to scan bridge's modal properties with vehicle frequencies and road roughness eliminated. Struct Control Health Monit 2022;e2968. https://doi.org/10.1002/stc.2968.

[29] Zhu XQ, Law SS. Structural Health Monitoring Based on Vehicle-Bridge Interaction: Accomplishments and Challenges. Adv Struct Eng 2015;18(12):1999–2015. https://doi:10.1260/1369-4332.18.12.1999.

[30] Malekjafarian A, McGetrick PJ, OBrien EJ. A review of indirect bridge monitoring using passing vehicles. Shock Vib 2015;2015:1–16. https://doi.org/10.1155/2015/286139.

[31] Yang YB, Yang JP. State-of-the-art review on modal identification and damage detection of bridges by moving test vehicles. Int J Struct Stab Dyn 2018;18(02): 1850025. https://doi.org/10.1142/s0219455418500256.

[32] Y.B. Yang J.P. Yang B. Zhang Y. Wu Vehicle Scanning Method for Bridges 2019 John Wiley and Sons Ltd London 10.1002/9781119539629.

[33] Shokravi H, Shokravi H, Bakhary N, Heidarrezaei M, Rahimian Koloor SS, Petrů M. Vehicle-assisted techniques for health monitoring of bridges. Sensors 2020;20(12): 3460. https://doi:10.3390/s20123460.

[34] Wang ZL, Yang JP, Shi K, Xu H, Qiu FQ, Yang YB. Recent advances in researches on vehicle scanning method for bridges. Int J Struct Stab Dyn 2022;22(15). https://doi.org/10.1142/s0219455422300051.

[35] Shi Z, Uddin N. Extracting multiple bridge frequencies from test vehicle – a theoretical study. J Sound Vib 2021;490:115735. https://doi.org/10.1016/j.jsv.2020.115735.

[36] Shi Z, Uddin N. Theoretical vehicle bridge interaction model for bridges with non-simply supported boundary conditions. Eng Struct 2021;232:111839. https://doi.org/10.1016/j.engstruct.2020.111839.

[37] Xu H, Liu YH, Wang ZL, Shi K, Zhang B, Yang YB. General contact response of single-axle two-mass test vehicles for scanning bridge frequencies considering suspension effect. Eng Struct 2022;270:114880. https://doi.org/10.1016/j.engstruct.2022.114880.

[38] Popov VL. Contact Mechanics and Friction 2017. https://doi.org/10.1007/978-3-662-53081-8.

[39] Paz M, Leigh W. Structural Dynamics: Theory and Computation, 5th Edition. New York: Springer Science & Business Media, Inc; 2004. https://doi.org/10.1007/978-1-4615-0481-8.

[40] Behroozinia P, Khaleghian S, Taheri S, Mirzaeifar R. An investigation towards intelligent tyres using finite element analysis. Int J Pavement Eng 2018;21(3): 311–21. https://doi.org/10.1080/10298436.2018.1475664.

[41] The Hilbert Transform. Handbook of Formulas and TABLEs for Signal Processing 2018; 15–1–15–27. https://doi:10.1201/9781315219707-15.

[42] Wang Z-C, Ren W-X, Chen G-D. A Hilbert transform method for parameter identification of time-varying structures with observer techniques. Smart Mater Struct 2012;21(10):105007. https://doi.org/10.1088/0964-1726/21/10/105007.

[43] Barker RM, Puckett JA. Design of highway bridges: An LRFD approach. John Wiley & Sons. (2013). https://doi.org/10.1002/9781118411124.

[44] MATLAB, Version R2022a (9.12.0.1884302), 64-bit (win64). The MathWorks Inc., 1984-2022.